The Meteoritical Society

Meteoritics & Planetary Science 41, Nr 12, 1959–1987 (2006)
Abstract available online at http://meteoritics.org

Differentiation and evolution of the IVA meteorite parent body: Clues from pyroxene geochemistry in the Steinbach stony-iron meteorite

Alex RUZICKA* and Melinda HUTSON

Cascadia Meteorite Laboratory, Department of Geology, Portland State University,
Department of Geology, 17 Cramer Hall, 1721 Southwest Broadway, Portland, Oregon 97207–0751, USA
*Corresponding author. E-mail: ruzickaa@pdx.edu

(Received 18 December 2005; revision accepted 02 October 2006)

Abstract–We analyzed the Steinbach IVA stony-iron meteorite using scanning electron microscopy (SEM), electron microprobe analysis (EMPA), laser ablation inductively-coupled-plasma mass spectroscopy (LA-ICP-MS), and modeling techniques. Different and sometimes adjacent low-Ca pyroxene grains have distinct compositions and evidently crystallized at different stages in a chemically evolving system prior to the solidification of metal and troilite. Early crystallizing pyroxene shows evidence for disequilibrium and formation under conditions of rapid cooling, producing clinobronzite and type 1 pyroxene rich in troilite and other inclusions. Subsequently, type 2 pyroxene crystallized over an extensive fractionation interval. Steinbach probably formed as a cumulate produced by extensive crystal fractionation (~60–70% fractional crystallization) from a high-temperature (~1450–1490 °C) silicate-metallic magma. The inferred composition of the precursor magma is best modeled as having formed by ≥30–50% silicate partial melting of a chondritic protolith. If this protolith was similar to an LL chondrite (as implied by O-isotopic data), then olivine must have separated from the partial melt, and a substantial amount (~53–56%) of FeO must have been reduced in the silicate magma. A model of simultaneous endogenic heating and collisional disruption appears best able to explain the data for Steinbach and other IVA meteorites. Impact disruption occurred while the parent body was substantially molten, causing liquids to separate from solids and oxygen-bearing gas to vent to space, leading to a molten metal-rich body that was smaller than the original parent body and that solidified from the outside in. This model can simultaneously explain the characteristics of both stony-iron and iron IVA meteorites, including the apparent correlation between metal composition and metallographic cooling rate observed for metal.

INTRODUCTION

The IVA iron meteorites are generally agreed to have formed by fractional crystallization in an asteroidal core-forming environment (Scott et al. 1996; Wasson and Richardson 2001; Wasson et al. 2006), but they present several puzzles. One is how to reconcile the presence in four IVA irons of silicate minerals that would have tended to separate from dense metallic metal. Two of these silicate-bearing IVAs (Steinbach and São João Nepomuceno) contain a distinctive assemblage of low-Ca pyroxene and tridymite, and contain so much silicate (>50 vol%) that they can be properly termed stony-iron meteorites (Ulff-Møller et al. 1995; Scott et al. 1996; Haack et al. 1996; Wasson et al. 2006). The other two, Gibeon and Bishop Canyon, contain rare but sometimes coarse inclusions of tridymite and quartz (Ulff-Møller et al. 1995; Scott et al. 1996; Marvin et al. 1997; Wasson et al. 2006). These silicate-bearing IVAs have metal compositions that are typical of the many IVA irons that lack silicate, so they appear to be samples of the same parent body (or bodies) that produced other IVA irons (Scott et al. 1996; Wasson et al. 2006).

Another puzzle of IVA irons is how to explain their order-of-magnitude variations in metallographic cooling rates (Goldstein and Short 1967; Moren and Goldstein 1978, 1979; Rasmussen et al. 1995; Yang et al. 2006). It is difficult to understand how large variations in cooling rate could arise in a metal core surrounded by a silicate mantle, as this thermal environment would be expected to result in uniform temperatures within the core (Schaudy et al. 1972; Moren and Goldstein 1978, 1979; Haack and Scott 1992; Haack et al. 1996; Wasson and Richardson 2001). Moreover, the derived cooling rates correlate with the bulk Ni content of the metal (Moren and Goldstein 1978, 1979; Rasmussen et al. 1995)

and thus with the extent of fractional crystallization (Scott et al. 1996; Yang et al. 2006). In general, the lower the Ni content in IVAs, the less fractional crystallization and the more rapid the cooling rate. It has not been clear why cooling rates would vary with Ni content in this way (e.g., Moren and Goldstein 1978, 1979; Haack et al. 1996; Wasson and Richardson 2001).

Various explanations have been offered for the large variations in metallographic cooling rates: 1) they could be an artifact caused by errors in the cooling rate technique (Wasson and Richardson 2001; Wasson et al. 2006); 2) they could represent the formation of IVAs in different parent bodies (Schaudy et al. 1972; Rasmussen 1982); or 3) they could represent the formation of IVAs in different pods or fragments inside a single silicate-rich parent body (Moren and Goldstein 1978, 1979; Rasmussen et al. 1995; Haack et al. 1996). Each of these interpretations is problematic and cannot explain the apparent Ni-cooling rate correlation. If they are an artifact, why is the correlation so systematic and not seen in other iron meteorites? If IVAs originated in multiple parent bodies, wouldn't a randomized Ni-cooling rate distribution be more likely than having a single correlation? If the IVAs formed out of separate metal pods within a larger silicate-rich body, why would metal differentiation be correlated with cooling environment, and why is there not more silicate associated with these pods (why are silicate-bearing IVAs so uncommon)? Another alternative, proposed by Haack et al. (1996), is that the Ni-cooling rate correlation is real, but merely a chance occurrence with no special significance caused by the sampling of a small number of metal-rich pods. This is also not satisfying because it has a very low probability, as Haack and coworkers (1996) themselves showed. Our preferred explanation, which was also recently proposed by Yang et al. (2006) independently, is that the IVA core had lost its silicate mantle during an impact event.

The final distinctive feature of at least the stony-iron IVAs is their apparently unusual thermal history, with different cooling rates at different temperatures. The better-studied Steinbach is illustrative. A small amount of the low-Ca pyroxene in Steinbach is disordered clinobronzite (Reid et al. 1974; Ulff-Møller et al. 1995; Haack et al. 1996), which is inferred to have formed by rapid cooling at high temperatures (Reid et al. 1974), on the order of ~100 °C/h at ~1200 °C (Haack et al. 1996). On the other hand, much lower cooling rates ($\leq 2 \times 10^{-6}$ °C/h) have been estimated for Steinbach at lower temperatures (≤1000 °C) based on different methods. These include cooling rates on the order of ~980 °C/Myr at ~1000 °C based on oxygen-isotope thermometry (Wang et al. 2004), ~20 °C/Myr at <700 °C based on the composition and width of taenite lamellae in metal (Rasmussen et al. 1995; Haack et al. 1996), and ~18,000 °C/Myr at ~430–470 °C based on Fe-Mg ordering in orthopyroxene (Ganguly and Stimpfl 2000). Recently, Goldstein and coworkers have re-evaluated metallographic cooling rates of Steinbach and derive a value of ~150 °C/Myr (Yang et al., Forthcoming).

Given the large apparent difference in cooling rate for Steinbach at high and low temperatures, and the large variations in metallographic cooling rates, Haack et al. (1996) suggested that IVA irons could have formed by catastrophic collisional disruption and reassembly of hot core and mantle fragments. This process could have resulted in rapid cooling rates during parent body disruption and much slower cooling rates after reassembly of the body. Although this model is difficult to reconcile with all of the inferred cooling rates (e.g., Ganguly and Stimpfl 2000; Wang et al. 2004), it has received support (Haack et al. 1996; Scott et al. 1996; Wang et al. 2004).

It is apparent that the silicate-bearing IVAs, although small in number, may place important constraints on the origin of the entire IVA parent body. In this study, we focus on a better understanding of the petrology of the silicates in Steinbach, using optical microscopy and scanning electron microscopy (SEM), electron microprobe analysis (EMPA), laser ablation inductively-coupled-plasma mass spectroscopy (LA-ICP-MS), and modeling techniques. Most of our attention centers on the geochemistry of low-Ca pyroxene in the meteorite. Among IVAs, Steinbach has an intermediate-to-high Ni content in metal and among the lowest apparent metallographic cooling rate (Rasmussen et al. 1995; Scott et al. 1996; Haack et al. 1996), presumably indicative of metal that crystallized from an evolved, well-insulated metallic magma. The origin of the silicate fraction in Steinbach and other IVAs is uncertain. Previous workers have suggested that the stony irons crystallized from Si-rich magma that was injected into a partially molten metallic core by solidification shrinkage of the core (Ulff-Møller et al. 1995), by injection of silicate impact melt into a previously solidified core (Wasson et al. 2006), or by the melting of entrained silicate fragments mixed with hot metal after catastrophic collisional disruption and reassembly of the parent body (Scott et al. 1996). Scott et al. (1996) also suggested that the stony-iron IVAs could have formed as cumulates near the core-mantle boundary, possibly analogous to pallasites, although they noted that the Si-oversaturated composition of the silicates is not readily explained by this model. Regardless of how the IVAs originated, we make the assumption that they formed out of a protolith that was chemically similar to an ordinary chondrite, based primarily on the oxygen-isotope compositions of the silicates, which match those in L and LL chondrites (Clayton et al. 1983; Wang et al. 2004). Although recent evidence for a late origin of chondrite parent bodies (e.g., Bizzarro et al. 2005) may rightly lead one to question the validity of this assumption, all meteorite parent bodies were probably broadly chondritic in composition initially, and derivation of the IVAs from a low-iron ordinary chondrite protolith is the simplest interpretation, as it is mutually consistent both with the oxygen isotopic

composition of silicates and with the chemical composition of silicates and metal (Wasson et al. 2006).

ANALYTICAL METHODS

Four polished thick sections (~0.1–0.2 mm thick) were prepared from adjacent pieces of Steinbach (6.23 kg Breitenbach mass from the British Museum) and were used for optical and SEM petrography, EMPA, and LA-ICP-MS.

Modal data were obtained by manual point counting of reflected light images, using Photoshop to create mosaics and overlay grids on the mosaics. Uncertainties for the modes were estimated using the formulas of Solomon (1963) and are described in detail elsewhere (Ruzicka et al. 2006). SEM work was performed at Portland State University using a JEOL JSM-35C with a Kevex energy dispersive detector and 4pi digital image/spectrum acquisition system. EMP analyses of low-Ca pyroxene, tridymite, and chromite were obtained at Oregon State University using a Cameca SX-100 electron microprobe equipped with five wavelength dispersive spectrometers. Well-characterized mineral and glass standards were used. An accelerating voltage of 15 KV, a 50 nA sample current, and a beam focused to an ~1 μm diameter were used for all analyses. Count times on X-ray peaks were 10 s for Si and Mg, 30 s for Na, and 55–60 s for other elements (Al, Ca, Ti, Mn, Cr, Fe, Ni). Detection limits (1σ) for the analyses calculated using Cameca-supplied software are ~0.01 wt% for Na_2O, MgO, Al_2O_3, CaO, and TiO_2; ~0.02 wt% for SiO_2 and MnO; and ~0.03–0.04 wt% for Cr_2O_3, FeO, and NiO.

LA-ICP-MS analyses were performed using a VG Elemental PQ ExCell quadrupole ICP-MS fitted with a VG Merchantek UV193 Laserprobe ArF excimer laser in the W. M. Keck Collaboratory for Plasma Spectrometry at Oregon State University. The laser was operated with 4 Hz pulse times, a forward power of 1340 W, and an effective spot diameter on the samples of ~90 μm. Helium gas flowing over the sample was used to carry the ablation effluent to the ICP-MS. Most analyses were obtained in "point mode" which included an initial 45 s of "pre-shot" background counts, 40 s of counts during pulsed laser firing shots, and counts obtained during a final 45 s "washout" time. Some analyses were obtained in "traverse" mode, in which the pre-shot and washout times were reduced for sequential shots. Measured species included isotopes of 36 elements with strong lithophile tendencies. Analyses of unknowns (low-Ca pyroxene, tridymite, chromite, and some test analyses of troilite and FeNi metal) were interleaved with analyses of glass standards (NIST 612, BCR-2G, and BHVO-2G) in the same shift. No significant counts could be obtained on tridymite, apparently owing to poor coupling between the laser and this mineral. For metal, significant counts for Ni and Co were observed, whereas for troilite, significant counts were obtained for Ni, Mn, Co, Cr, and V.

For each LA-ICP-MS analysis, raw counts for measured species (isotopes) were recorded every ~410 ms. These data were used for time-series analysis and were converted to concentrations using off-line spreadsheet programs. The pattern of count rates for each isotope was examined to set appropriate time intervals for backgrounds and peaks and to calculate background-corrected (net) count rates (N), which were related to concentrations (C) using the following expression:

$$(C_i/N_i)_{unk} = (C_i/N_i)_{NIST} \times (C_{ref}/N_{ref})_{unk} \times (N_{ref}/C_{ref})_{NIST} \quad (1)$$

where *unk* = the unknown, *NIST* = the NIST 612 standard, *i* = an isotope of the element of interest, and *ref* = an isotope of a reference element (Si for pyroxene or glass; Cr for chromite). For $(C_i)_{NIST}$ and $(C_{ref})_{NIST}$, the preferred average concentration values of Pearce et al. (1997) were used, and for $(C_{ref})_{unk}$, the average concentrations of Si in pyroxene and Cr in chromite as determined by prior EMP analysis were assumed.

Table A1 (Appendix) gives data for the glass standards and for low-Ca pyroxene in Steinbach that are relevant for evaluating LA-ICP-MS analysis quality. The "3σ detection limit" (DL) is related to three times the standard deviation (3σ) of background count rates on the NIST 612 glass, and is calculated by:

$$DL = (C_i/N_i)_{NIST} \times (3\sigma)_{bkgd} \quad (2)$$

where *bkgd* refers to background count rates on this glass. Similar values of 3σ are observed for background counts on different phases, suggesting that Expression 2 represents a meaningful estimate of the true detection limit on unknowns. Typical values of DL for trace elements are ~0.5–15 ng/g (Table A1). Estimates of precision and accuracy were obtained by analyzing the BCR-2G and BHVO-2G secondary glass standards as unknowns, with the precision related to the coefficient of variation obtained in repeat analyses, and the accuracy related to the difference of the measured concentrations and reported concentrations. Reported concentrations in these secondary standards for most elements were taken from the USGS (see http://minerals.cr.usgs.gov/geo_chem_stand), and for the rare earth elements (REE) from Kent et al. (2004). Table A1 shows that for most elements, precisions are on the order of ~1–10%. The accuracies are of the same order as the precisions for BHVO-2G, but typically are worse for BCR-2G, probably because the reported concentrations for the latter are more poorly determined. The counting error for any given element is related to the expected counting statistic error, given by $\sqrt{N}/N$, where N = net count rate. The counting uncertainty for most trace elements in low-Ca pyroxene is on the order of ~2–20 ng/g (Table A1).

The concentrations for some trace elements in Steinbach low-Ca pyroxene proved to be very low, often below or close to the detection limit. Consequently, additional criteria were

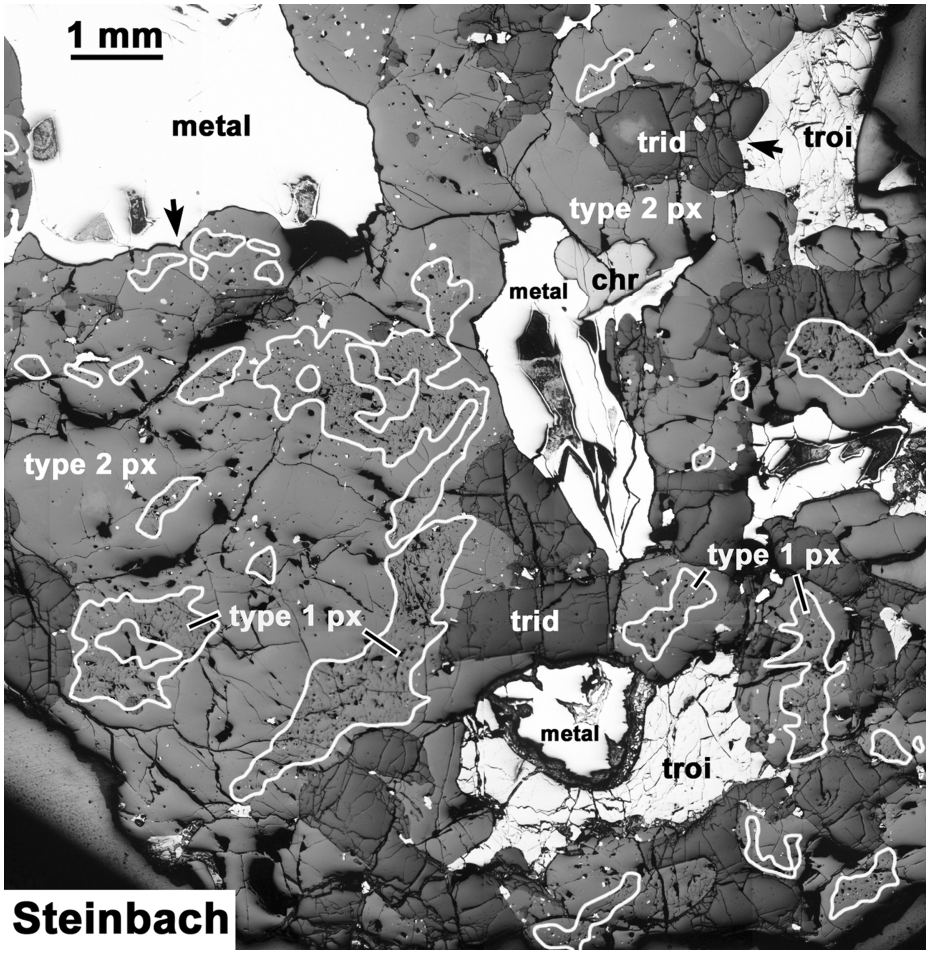

Fig. 1. A reflected light image mosaic of Steinbach showing pyroxene (px = medium gray), tridymite (trid = dark gray), metal (white), troilite (troi = nearly white), and a single cluster of chromite grains (chr = bright gray). Type 1 pyroxene contains more pits, and fine-scale cracks and inclusions (more resolvable on higher-magnification images) than type 2 pyroxene; contacts between type 1 and type 2 pyroxene are convolute, and often type 1 pyroxene is surrounded by type 2 pyroxene (e.g., at lower right). Troilite and metal fill grain interstices of silicates (e.g., dark arrows upper left and upper right). This area of Steinbach (a portion of section ST3A) contains an atypically large amount of type 1 pyroxene.

used to identify whether low apparent concentrations represented positive detections. Selection criteria were applied to remove from consideration those elements in any given analysis that were above the background but that had large (>50%) counting errors, or that had large (>200% relative standard deviation) variations in net, normalized count rates within six even time intervals (subsets) in the peak interval. Large subset deviations reflect either poor counting statistics or the presence of sporadic inclusions in the analysis volume. Use of these criteria improved the overall quality of the data set by excluding suspect values.

RESULTS

Textures and Mode

Steinbach contains millimeter-size grains and clusters of low-Ca pyroxene, tridymite, and chromite as well as millimeter- to-centimeter-size grains of metal and troilite (Figs. 1 and 2). Apparent grain outlines and differences in internal textures suggest that much of the pyroxene is glomerocrystic, composed of intergrown grains (Figs. 1, 2d, and 2e). Both coarse metal and troilite grains fill interstices or cusps (Scott et al. 1996) between intergrown pyroxene and tridymite grains (Figs. 1 and 2d).

Three types of pyroxene are identified based on their appearance in reflected light (Fig. 1) and backscattered electron (BSE) images (Fig. 2). Type 1 pyroxene contains many small-scale pits and cracks and small (often <10 μm in diameter) inclusions, giving it a cloudy appearance (Figs. 1 and 2). Most inclusions are troilite, but metal and tridymite have also been identified (Fig. 2b). Other inclusions consist of chromite and Fe-Si silicates (Ulff-Møller et al. 1995; Wasson et al. 2006). These inclusions are randomly distributed within type 1 grains. The pits in type 1 grains are typically similar in size or larger than the inclusions, and we suggest that plucking

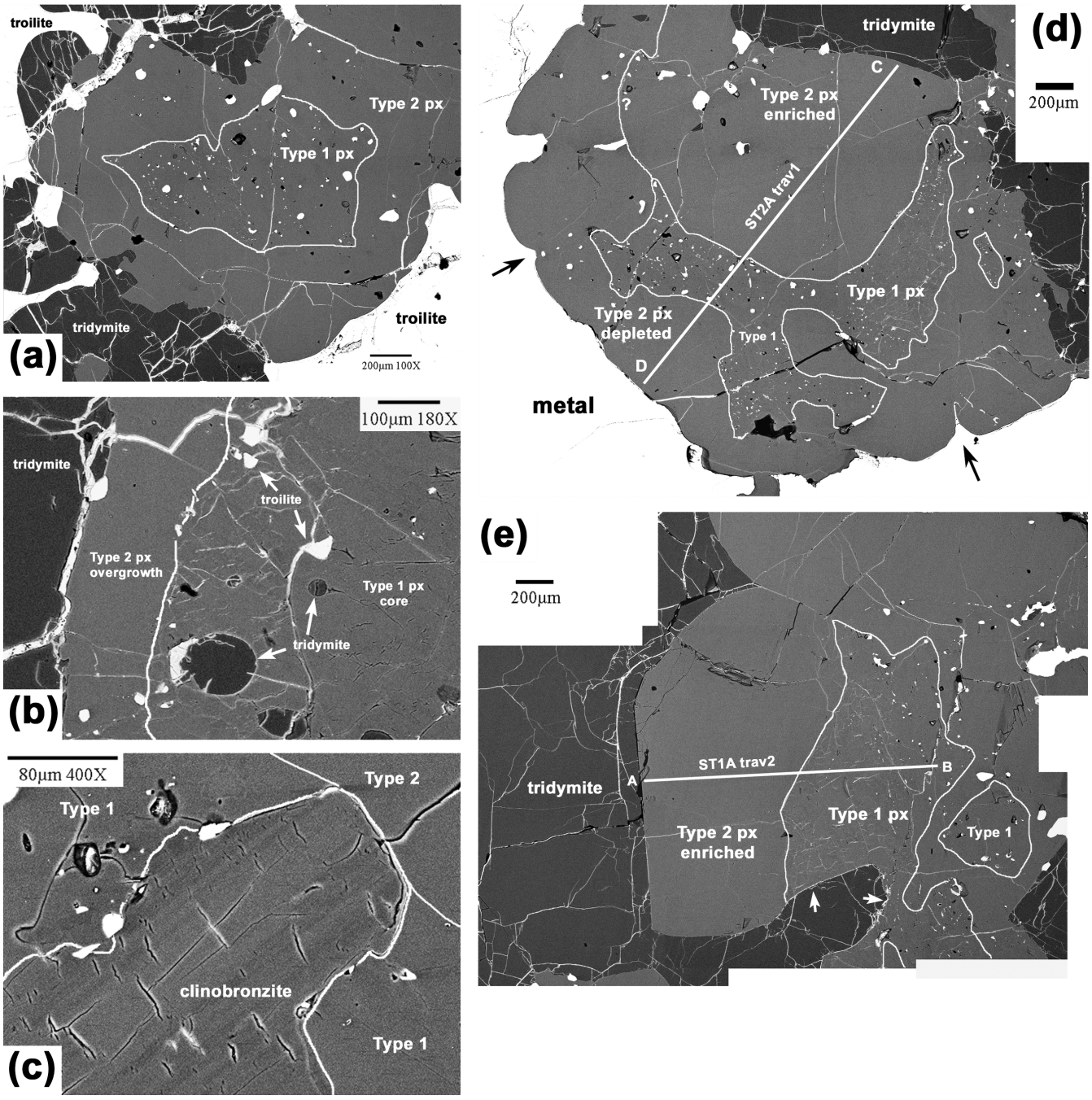

Fig. 2. Backscattered electron (BSE) images of Steinbach. a) Inclusion-poor type 2 pyroxene enveloping an inclusion-rich and pitted type 1 pyroxene core. Most inclusions in pyroxene consist of troilite. b) A close-up showing type 2 pyroxene overgrowth surrounding a type 1 pyroxene core. Inclusions in the type 1 pyroxene consist of troilite, tridymite, and metal. Inclusions are more abundant in the outer zone of the type 1 pyroxene core, near the overgrowth. c) Pyroxene is identified as clinobronzite by its faint lamellar zoning and small cracks oriented roughly perpendicular to the lamellae. This clinobronzite is enclosed within type 1 pyroxene that itself is surrounded by type 2 pyroxene. d) An image mosaic showing a pyroxene cluster containing type 1 and apparent different generations of type 2 pyroxene grains (depleted = Ca, Al-poor; enriched = Ca, Al-rich). Coarse metal fills cusps between apparently separate pyroxene grains that are intergrown (arrows). Line C-D shows the trace of an electron microprobe profile (Fig. 4b). e) A mosaic showing a pyroxene cluster containing both type 1 and type 2 pyroxene. Tridymite both fills cusps between type 2 pyroxene (upper left) and atypically occurs in direct contact with type 1 pyroxene without intervening type 2 pyroxene (arrows). Line A-B shows the trace of an electron microprobe (Fig. 4a) and subsequent LA-ICP-MS profile (Fig. 8c). A portion of this type 1 pyroxene (left occurrence) contains faint lamellar zoning and may be clinobronzite; it is unusually depleted in Y and may be relict. Px = pyroxene.

Table 1. The modal compositions of three sections of Steinbach, compared to literature values.[a]

				This study[b]	Literature[c]	
	ST1A	ST2A	ST3A		(1)	(2)
vol%						
Type 1 pyroxene[d]	2.4 (1.6)	1.6 (1.6)	4.3 (1.8)	3.1	4.5	1.6
Type 2 pyroxene[d]	42.9 (6.6)	39.2 (8.1)	40.8 (5.5)	41.2	37.3	38.0
Tridymite	19.6 (4.5)	20.7 (5.9)	30.1 (4.7)	24.7	20.2	20.8
Chromite	0.5 (0.7)	0	0.5 (0.6)	0.4	–	0
Troilite	6.2 (2.5)	2.8 (2.2)	10.0 (2.7)	7.2	5.7	6.6
Fe,Ni metal	28.6 (5.4)	35.8 (7.8)	14.3 (3.3)	23.4	32.4	32.2
Total	100.2	100.1	100.0	100.0		
Px/(px + trid)[e]	0.77	0.74	0.68	0.72	0.75	0.73
N	3978	5920	4399	14,297	3326	6949
s (μm)	251	160	281			
Area mapped (mm^2)	250	151	349	750	1230	1794

[a]All data were obtained by point counting. *N* = number of points; *s* = grid spacing; area mapped approximated by $N * s^2$. Values in parentheses represent 1σ errors and assume a representative grain diameter of 1.0 mm.

[b]Area-weighted average.

[c]Literature: (1) Ulff-Møller et al. (1995); (2) Scott et al. (1996).

[d]Type 1 pyroxene: rich in pits, microcracks, and small (<10 μm in diameter) inclusions of troilite. Type 2 pyroxene: "normal" in containing relatively few pits, cracks, or small troilite inclusions. Type 1 and type 2 pyroxene in this study equated to clinobronzite and orthobronzite, respectively, of Ulff-Møller et al. (1995) and Scott et al. (1996).

[e]Total pyroxene/(total pyroxene + tridymite) weight ratio, assuming a density of 3.35 g/cm^3 for pyroxene and 2.33 g/cm^3 for tridymite (based on values given in Gaines et al. 1997).

during sample preparation could have been partially responsible for creating them. In contrast, type 2 pyroxene is not pitted or cracked on a fine scale and contains fewer small inclusions (Figs. 1, 2a, and 2d). Type 2 pyroxene often encloses or forms overgrowths on type 1 pyroxene (Figs. 1, 2a, and 2b), and usually but not always separates type 1 pyroxene from tridymite (Figs. 1, 2a, 2d, and 2e). The contacts between type 1 and 2 pyroxene are often convolute (Figs. 1, 2a, 2d, and 2e). Finally, a small amount of the pyroxene was identified in BSE images as clinobronzite by the presence of faint lamellar zoning and crack-like features generally perpendicular to the lamellae (Fig. 2c). The clinobronzite in Steinbach contains some small inclusions and is both cracked and pitted, and resembles type 1 pyroxene in reflected light. As the lamellar zoning that was used to identify clinobronzite is faint, it may have been overlooked, and some of our type 1 pyroxene may consist of clinobronzite. In some areas, clinobronzite is enclosed by even more inclusion-rich type 1 pyroxene (Fig. 2c), which itself is enclosed in type 2 pyroxene. In contrast to pyroxene, tridymite is notably depleted in inclusions (Fig. 2e) (Wasson et al. 2006). Chromite grains sometimes contain inclusions of tridymite.

Table 1 shows modal data for three sections of Steinbach studied in this work compared to two previous determinations. The total area we examined was less than that of previous workers, but the total number of points we counted was much larger, suggesting that our data should be relatively representative and accurate for finer-grained phases such as pyroxene, tridymite, and chromite, and probably less accurate and representative for metal and troilite. All data suggest that Steinbach contains ~40 vol% pyroxene and ~20–30% tridymite, with the remainder of the meteorite consisting mainly of metal and troilite (Table 1). The pyroxene/(pyroxene + tridymite) weight ratio is well-constrained at ~0.7–0.8 (Table 1). The mode we determined for type 1 pyroxene (1.6–4.3 vol%), which includes the small amount of pyroxene we unambiguously identified as clinobronzite, is similar to the amount of clinobronzite identified in transmitted light by previous workers (Table 1) and probably represents the same phase. The amount of troilite and metal is highly variable in each of our sections, although the average amount of troilite in our samples is similar to what was found by others in larger slices (Table 1). The variability of metal and troilite in our sections is almost certainly the result of the difficulty in obtaining representative data for such coarse phases.

Phase Chemistry

EMPA Data

Table 2 shows average compositions of pyroxene, tridymite, and chromite in Steinbach, and Table 3 shows the composition of different subtypes of pyroxene (clinobronzite, type 1, type 2).

Overall, low-Ca pyroxene in Steinbach shows small variations in MgO and FeO contents (Table 2). Nonetheless, Fs and Wo values are generally correlated with one another, and there is a continuum in composition from ~$Fs_{15.5}Wo_{0.1}$ to ~$Fs_{19}Wo_1$ (Fig. 3). There is no evidence in our data set for a hiatus in Wo contents between different pyroxene types (Fig. 3), in contrast to what was found by previous workers

Table 2. Composition of low-Ca pyroxene, tridymite, and chromite in Steinbach, determined by electron microprobe analysis.[a]

	Low-Ca pyroxene $N = 258$		Tridymite $N = 55$		Chromite[b] $N = 6$	
wt%	Mean ± std	Range	Mean ± std	Range	Mean ± std	Range
SiO_2	55.4 ± 1.0	57.3–52.9	98.5 ± 1.1	100.4–96.2	0.03 ± 0.02	0.04–0.01
TiO_2	0.02 ± 0.01	0.09–<0.01	0.02 ± 0.01	0.03–0.01	0.12 ± 0.01	0.13–0.12
Al_2O_3	0.26 ± 0.07	0.41–0.10	0.26 ± 0.04	0.30–0.10	3.15 ± 0.22	3.36–2.74
Cr_2O_3	0.54 ± 0.11	0.77–0.27	0.01 ± 0.01	0.09–<0.01	65.4 ± 0.3	66.0–65.1
FeO	11.4 ± 0.35	13.3–9.98	0.11 ± 0.10	0.55–<0.01	24.5 ± 0.2	24.9–24.3
MnO	0.49 ± 0.04	0.59–0.39	0.01 ± 0.01	0.04–<0.01	0.85 ± 0.19	1.24–0.70
MgO	31.3 ± 0.7	33.2–29.4	<0.01	0.02–<0.01	5.89 ± 0.21	6.20–5.57
CaO	0.34 ± 0.16	0.59–0.06	<0.01	0.09–<0.01	<0.01	<0.01
Na_2O	0.01 ± 0.01	0.03–<0.01	0.05 ± 0.02	0.08–0.02	<0.01	0.01–<0.01
NiO	0.04 ± 0.04	0.41–<0.01	0.03 ± 0.02	0.07–<0.01	<0.01	0.07–<0.01
Total	99.9		98.9		100.0	
mol%						
Wo	0.64 ± 0.30	1.11–0.12	–	–	–	–
En	82.4 ± 0.8	85.1–80.2	–	–	–	–
Fs	16.9 ± 0.6	19.4–14.7	–	–	–	–

[a]N = number of points; std = standard deviation.
[b]Chromite analyses were normalized to 100% before averaging; original analysis totals were between 101.6–103.5.

(Reid et al. 1974; Ulff-Møller et al. 1995). We suggest that the apparent hiatus seen by previous workers is illusory and an artifact of the smaller data sets that were used. Significant variations are seen for the concentrations of Al_2O_3, Cr_2O_3, and CaO (Table 2).

Based on EMPA data, type 1 and clinobronzite grains have indistinguishable compositions (Table 3). Collectively, these grain types have compositions generally similar to subgroups "a" (orthobronzite) and "a*" (clinobronzite), identified by Ulff-Møller et al. (1995). Type 2 grains have more variable Al, Ca, and Cr contents (Table 3), with the most enriched of these appearing to correspond to the "b" subgroup (orthobronzite) identified by Ulff-Møller and coworkers (1995).

Microprobe data for pyroxene grains indicate limited intragranular zoning. The most significant zoning occurs for type 2 grains, which commonly have Wo-rich (~1 mol%) and Cr_2O_3-rich (~0.6–0.7 wt%) interiors and margins depleted in these components (Table 3; Fig. 4). The depletions occur over differing spatial extents: ~100–200 μm wide for Ca, and ~100–500 μm wide for Cr. Other type 2 grains have lower Wo and Cr_2O_3 contents in their interiors and are not significantly zoned.

In contrast, adjacent pyroxene grains in the same cluster can have significantly different compositions. For example, Fig. 4a shows a microprobe traverse across adjacent type 2 and type 1 grains which differ significantly in Al_2O_3 and Wo contents and more subtly in En content, despite having fairly uniform concentrations in each portion. (The spike in NiO content is probably an artifact caused by proximity to an inclusion.) Sharp chemical differences in Al, Ca, and Cr are also observed between different type 2 grains in the same

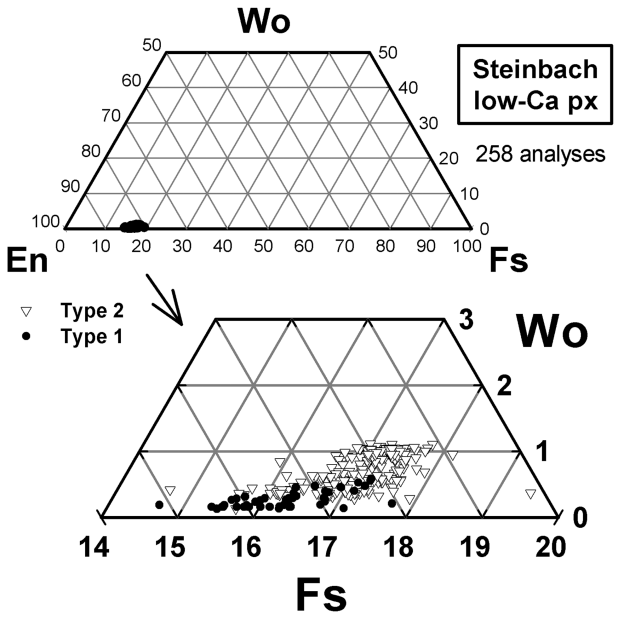

Fig. 3. Pyroxene quadrilateral showing EMPA data for low-Ca pyroxene. Type 1 pyroxene tends to have lower Wo and Fs contents than type 2 pyroxene, but the two overlap in composition.

pyroxene cluster (Fig. 4b). The large type 2 pyroxene on the left side of Fig. 4b is significantly enriched in Al_2O_3, Cr_2O_3, and CaO compared to the smaller type 2 pyroxene.

The compositions of tridymite and chromite (Table 2) are similar to those previously measured for IVA stony irons (Ulff-Møller et al. 1995; Scott et al. 1996), except that our Na_2O concentrations in tridymite are lower. This may be caused by volatility of sodium under the microprobe beam. In

Table 3. Composition of low-Ca pyroxene subtypes in Steinbach, determined by electron microprobe analysis[a].

	Clinobronzite $N = 7$	Type 1 pyroxene $N = 42$	Type 2 pyroxene $N = 211$	Type 2 cores[b] $N = 51$	Type 2 rims[b] $N = 17$
wt%	Mean ± std	Mean ± std	Mean ± std	Mean ± std	Mean ± std
SiO_2	56.5 ± 0.1	55.6 ± 0.9	55.4 ± 1.0	55.2 ± 1.1	55.5 ± 1.1
TiO_2	0.02 ± 0.01	0.01 ± 0.01	0.02 ± 0.01	0.02 ± 0.01	0.02 ± 0.01
Al_2O_3	0.21 ± 0.02	0.20 ± 0.03	0.28 ± 0.07	0.32 ± 0.02	0.34 ± 0.04
Cr_2O_3	0.45 ± 0.02	0.45 ± 0.08	0.56 ± 0.10	0.65 ± 0.03	0.54 ± 0.06
FeO	11.2 ± 0.3	11.1 ± 0.4	11.5 ± 0.3	11.6 ± 0.2	11.6 ± 0.3
MnO	0.49 ± 0.03	0.46 ± 0.04	0.50 ± 0.03	0.50 ± 0.03	0.49 ± 0.02
MgO	31.5 ± 0.3	32.0 ± 0.6	31.1 ± 0.7	30.8 ± 0.3	31.0 ± 0.4
CaO	0.15 ± 0.10	0.15 ± 0.06	0.38 ± 0.14	0.52 ± 0.04	0.37 ± 0.07
Na_2O	0.01 ± 0.01	0.01 ± 0.01	0.01 ± 0.01	0.01 ± 0.01	0.01 ± 0.01
NiO	0.05 ± 0.04	0.07 ± 0.08	0.04 ± 0.03	0.04 ± 0.03	0.04 ± 0.02
Total	100.6	100.0	99.8	99.6	99.9
mol%					
Wo	0.28 ± 0.20	0.28 ± 0.12	0.73 ± 0.27	0.99 ± 0.07	0.71 ± 0.13
En	83.1 ± 0.7	83.4 ± 0.7	82.2 ± 0.6	81.7 ± 0.2	82.1 ± 0.5
Fs	16.6 ± 0.5	16.3 ± 0.7	17.0 ± 0.5	17.3 ± 0.2	17.2 ± 0.5

[a]N = number of points; std = standard deviation.
[b]Subset of type 2 pyroxene subdivided into grain core or rim analyses.

tridymite the concentration of Al_2O_3 tends to be low on one or both grain margins, and FeO is usually enriched on grain margins. Similar zoning variations in tridymite were noted by others in both Steinbach and Gibeon, although alumina contents are significantly lower in Gibeon (Ulff-Møller et al. 1995; Scott et al. 1996).

LA-ICP-MS Data

Tables 4 and 5 summarize LA-ICP-MS data for pyroxene and chromite in Steinbach. Figure 5 shows CI-normalized abundances for individual pyroxene and chromite analyses, Figs. 6 and 7 show variation diagrams for key elements in pyroxene, and Fig. 8 illustrates pyroxene traverse data.

Trace-element compositions of clinobronzite and type 1 pyroxene are generally similar (Table 4). Analyses of these pyroxenes clearly reflect the effects of contamination by inclusions, most obviously for Ni and Co, but also for Zr, Rb, Ti, Zn, Ba, Hf, Th, U, V, Sc, Ga, and Sr. This contamination effect persists despite the efforts made to mitigate it (see the "Analytical Methods" section), and is best evaluated on an element-by-element basis using variation diagrams (see below). In contrast, the data for type 2 pyroxene are relatively free of inclusion contamination.

Trace-element data for core, mantle, and rim analyses in a representative type 2 pyroxene grain reveal little apparent core-to-rim zoning (Fig. 5a). However, in agreement with EMPA data, Ca and Cr are slightly enriched in the core compared to the grain rim. More subtle enrichments in the rim occur for Al, Ti, V, and Y. This and other grains are clearly LREE-depleted (La/Lu ~ 0.1 × CI chondrite).

Chromium, Zn, Nb, Ga, and V are strongly enriched in chromite compared to pyroxene, by factors of ~70–200 (Fig. 5; Tables 4 and 5). Compared to pyroxene, chromite is also enriched in Zr, Al, Ti, Hf, Th, and U (Fig. 5; Tables 4 and 5). As with pyroxene, there appears to be little chemical variability within chromite grains, although two grains differ slightly in Sc and Zr abundances (Fig. 5b).

Different type 2 pyroxene grains vary significantly in composition and form a continuous chemical trend (Table 4; Fig. 6). For type 2 pyroxene, the abundances of Ca, Cr, V, Y, Dy, Ti, Zr, and Sc vary directly with Al, whereas those of Mn and Co vary only slightly, and Ni shows a weak inverse relationship with Al content (Fig. 6 shows most of these elements). Although type 2 grains vary continuously in composition, it is convenient for discussion and tabulation purposes to refer to such grains as either "depleted" (with both ≤0.17 wt% Al and ≤0.15 wt% Ca) or "enriched" (up to 0.3 wt% Al and 0.4 wt% Ca). Besides Al and Ca, enriched type 2 grains have higher concentrations of well-determined incompatible elements (Sc, Ti, V, Y, Zr) (Table 4). Highly incompatible elements such as the LREE and Nb do not follow the expected pattern, but at the low concentrations at which these elements are found, precisions are too poor to resolve any chemical differences that may be present. In the discussion below, we therefore focus on those LA-ICP-MS data that have higher precision.

The compositions of type 1 pyroxene and clinobronzite overlap those of depleted type 2 grains for most elements, except that type 1 and clinobronzite grains are often apparently enriched in Ti, Zr, Sc, Co, and Ni (Fig. 6). The enrichments of these elements almost certainly reflect the presence of small inclusions, implying that the intrinsic trace element compositions of clinobronzite, type 1, and depleted type 2 pyroxenes are all similar.

The enrichments of Ti, Zr, and Sc in many type 1 pyroxenes compared to the type 2 trend (Fig. 6) cannot be

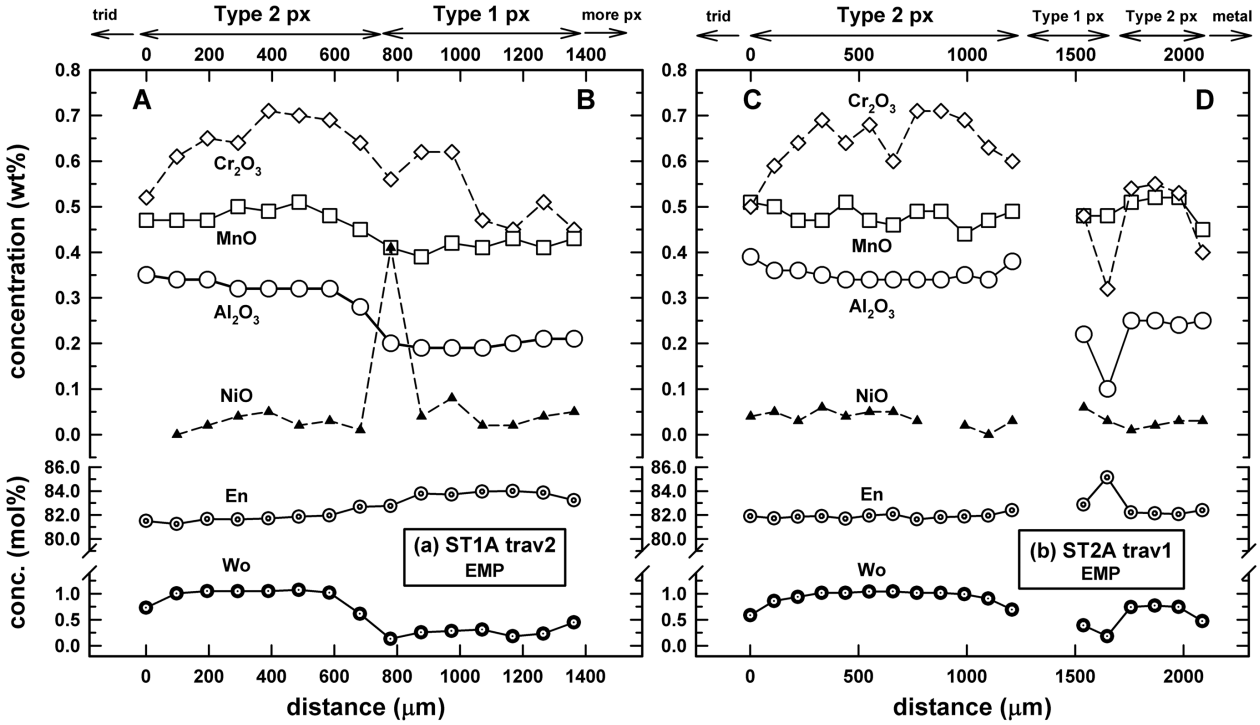

Fig. 4. Chemical profiles obtained by EMPA across: (a) composite type 2 and type 1 pyroxene grains (sample ST1A, traverse 2, shown in Fig. 2e), and (b) composite type 1 and type 2 grains of different compositions (sample ST2A, traverse 1, shown in Fig. 2d). The type 2 grains show characteristic depletions of Cr_2O_3 and Wo on their rims. Different pyroxene grains in the clusters have different compositions (especially evident for Al_2O_3). The gap in analyses in (b) reflects analyses that were excluded because of large inclusion contamination effects. Px = pyroxene, trid = tridymite.

attributed to metal or troilite inclusions as these elements do not correlate with either Co or Ni. Nor can they be attributed to chromite, as they do not correlate with Cr or V. However, the abundances of Ti, Zr, and Sc correlate with one another, suggesting that a different phase rich in all three elements is present as inclusions. One possibility is that this phase is ilmenite, which accommodates Zr (e.g., McKay et al. 1986; Green 1994) in addition to Ti.

Figure 6d reveals the presence of a Y-poor group of pyroxene that falls off the type 2 trend. The depletion of Y in these grains exceeds the 2σ count rate uncertainty and cannot be explained as an artifact of analyzing inclusions. Of 17 analyses of anomalously Y-poor pyroxene, 15 are of type 1 pyroxene, and one is for clinobronzite and one for type 2 depleted pyroxene.

Figure 7 shows the variation of Ni and Ga content with that of Co. These elements are partially siderophile and chalcophile, and both Ni and Co are concentrated in metal and troilite (see the "Analytical Methods" section). At high apparent Co contents (>25 μg/g), the concentration of Co correlates with that of Ni and Ga, whereas at lower Co contents (<10 μg/g), there is only a slight tendency for Co to vary directly with that of Ni and no apparent tendency to vary with that of Ga (Fig. 7). The high-Co analyses clearly reflect the effect of metal or troilite inclusions, whereas the low-Co "main field" analyses apparently reflect indigenous pyroxene compositions. These data suggest that pyroxene itself contains ~3–10 μg/g Co, ~1–40 μg/g Ni, and ~0.02–0.18 μg/g Ga.

LA-ICP-MS traverse data across different pyroxene grains in the same clusters are shown in Fig. 8. The main chemical gradients occur across grain boundaries in zones ~100–200 μm wide. For example, Fig. 8a shows adjacent depleted and enriched type 2 grains, with a factor of ~1.5–3 difference in the concentration of Cr, V, Sc, Ca, Al, Ti, Y, and Zr between the grains, much larger than the variations seen within the grains themselves. Figures 8b and 8c show similar or larger variations in Cr, V, Ca, Al, Ti, and Y concentration between type 1 and 2 grains, with the large variation in Y content (~5–10×) being especially notable. Cobalt and Zr are also apparently strongly enriched (~5–10×) in type 1 grains (Figs. 8b and 8c), but this is certainly an artifact caused by inclusions. Besides sharp differences in composition at grain boundaries, Fig. 8 also illustrates smaller chemical variations caused by intragranular zoning. These include depletions of Ca and Cr at the margins of type 2 grains adjacent to other grains of pyroxene, metal, or tridymite. Aluminum, Ti, and Y abundances are sometimes weakly enriched on type 2 grain margins adjacent to tridymite (e.g., Fig. 8c and the left side of Fig. 8b), but not always (e.g., the right side of Fig. 8b).

Table 4. Compiled LA-ICP-MS data for low-Ca pyroxene in Steinbach[a].

	Overall range	Clinobronzite	Type 1	Type 2 depleted	Type 2 enriched
		Mean ± std	Mean ± std	Mean ± std	Mean ± std
Al wt%	0.294–0.107 (143)	0.148 ± 0.007 (3)	0.142 ± 0.019 (25)	0.129 ± 0.016 (19)	0.215 ± 0.034 (96)
Si wt%	25.91 (143)	25.91 (3)	25.91 (25)	25.91 (19)	25.91 (96)
Ca wt%	0.410–0.0505 (143)	0.0780 ± 0.0195 (3)	0.0910 ± 0.0329 (25)	0.126 ± 0.012 (19)	0.287 ± 0.065 (96)
Sc µg/g	7.94–3.56 (143)	6.01 ± 0.51 (3)	5.28 ± 1.01 (25)	4.07 ± 0.34 (19)	5.28 ± 0.91 (96)
Ti µg/g	136–46.6 (143)	94.6 ± 6.8 (3)	85.1 ± 12.6 (25)	57.9 ± 8.7 (19)	99.5 ± 13.3 (96)
V µg/g	110–35.9 (141)	78.4 ± 6.7 (3)	64.0 ± 8.76 (25)	45.6 ± 10.2 (19)	79.5 ± 11.8 (94)
Cr wt%	0.463–0.214 (140)	0.308 ± 0.030 (3)	0.282 ± 0.037 (24)	0.257 ± 0.049 (19)	0.369 ± 0.039 (94)
Mn wt%	0.269–0.201 (143)	0.264 ± 0.007 (3)	0.225 ± 0.022 (25)	0.250 ± 0.016 (19)	0.259 ± 0.015 (96)
Co µg/g	333–2.9 (133)	33.6 ± 12.8 (2)	58.8 ± 70.1 (21)	5.2 ± 1.2 (19)	4.9 ± 1.2 (91)
Ni µg/g	2570–1.2 (108)	898 ± 230 (2)	1030 ± 731 (19)	38 ± 93 (12)[b]	21 ± 51 (75)[c]
Zn µg/g	1.52–0.22 (104)	n.d.	0.67 ± 0.24 (22)	0.45 ± 0.27 (19)	0.42 ± 0.12 (63)
Ga ng/g	280–22 (85)	110 ± 30 (3)	130 ± 70 (16)	100 ± 50 (14)	76 ± 3 (52)
Rb ng/g	600–14 (66)	170 ± 60 (3)	180 ± 160 (20)	95 ± 41 (4)	14 ± 14 (41)
Sr ng/g	120–9.2 (78)	35 ± 18 (2)	46 ± 28 (16)	37 ± 11 (8)	36 ± 19 (52)
Y ng/g	310–13 (141)	57 ± 55 (2)	72 ± 56 (24)	89 ± 15 (19)	170 ± 40 (96)
Zr ng/g	410–24 (131)	270 ± 67 (3)	220 ± 100 (24)	78 ± 40 (15)	130 ± 50 (89)
Nb ng/g	46–3.9 (93)	15 ± 7 (3)	14 ± 5 (20)	17 ± 7 (15)	16 ± 7 (55)
Cs ng/g	125–13 (67)	100 ± 5 (2)	60 ± 26 (21)	56 ± 17 (4)	44 ± 22 (40)
Ba ng/g	490–57 (48)	n.d.	230 ± 120 (13)	150 ± 40 (7)	210 ± 100 (28)
La ng/g	57–4.3 (48)	24 ± 11 (2)	22 ± 16 (8)	22 ± 15 (6)	19 ± 10 (32)
Ce ng/g	120–2.8 (120)	20 (1)	21 ± 23 (22)	20 ± 19 (12)	16 ± 8 (85)
Pr ng/g	16–2.1 (47)	9.6 (1)	7.2 ± 2.5 (11)	6.4 ± 2.4 (4)	6.6 ± 2.8 (31)
Nd ng/g	69–10 (73)	22 ± 0.3 (2)	21 ± 9 (8)	24 ± 10 (7)	29 ± 14 (56)
Sm ng/g	62–13 (39)	29 (1)	27 ± 10 (8)	36 ± 14 (5)	33 ± 15 (25)
Eu ng/g	18–4.7 (25)	7.4 (1)	8.2 ± 3.7 (7)	14 ± 4 (4)	10 ± 4 (13)
Gd ng/g	190–1.6 (44)	n.d.	78 ± 45 (12)	78 ± 29 (5)	75 ± 33 (27)
Tb ng/g	13–2.4 (54)	6.3 (1)	4.8 ± 2.2 (7)	4.8 ± 2.0 (7)	6.8 ± 2.8 (39)
Dy ng/g	67–8.6 (108)	28 (1)	21 ± 11 (12)	19 ± 4 (10)	33 ± 12 (85)
Ho ng/g	18–2.1 (84)	3.4 (1)	6.4 ± 2.7 (5)	6.3 ± 2.7 (9)	8.1 ± 3.7 (69)
Er ng/g	75–6.1 (111)	16 (1)	20 ± 7 (11)	21 ± 7 (9)	25 ± 12 (90)
Tm ng/g	13–2.4 (69)	4.2 (1)	5.3 ± 1.8 (15)	4.8 ± 2.1 (6)	7.0 ± 2.5 (47)
Yb ng/g	66–10 (102)	22 ± 2 (2)	28 ± 15 (11)	29 ± 13 (12)	35 ± 14 (77)
Lu ng/g	16–1.9 (78)	8.4 (1)	7.3 ± 2.3 (13)	9.4 ± 3.6 (8)	7.9 ± 3.3 (56)
Hf ng/g	28–7.7 (68)	18 ± 0.1 (2)	19 ± 6 (15)	14 ± 8 (4)	16 ± 5 (47)
Th ng/g	23–3.2 (15)	7.7 (1)	13 ± 8 (3)	8.9 ± 8.1 (5)	5.6 ± 3.3 (6)
U ng/g	6.8–1.3 (16)	3.5 ± 3.0 (2)	3.7 ± 1.7 (6)	2.6 ± 0.5 (3)	1.6 ± 0.2 (4)

[a]std = standard deviation. n.d. = not detected. Values in parentheses refer to the number of analyses averaged or included in range. Type 2 pyroxene that has low contents of Al (≤0.17 wt%) and Ca (≤0.15 wt%) is designated as "depleted," and otherwise is designated as "enriched." All data are normalized to the average Si concentration in low-Ca pyroxene determined by electron microprobe analysis.

[b]Best estimate of inclusion-free composition: Ni = 11 ± 8 µg/g.

[c]Best estimate of inclusion-free composition: Ni = 10 ± 10 µg/g.

DISCUSSION

Crystallization History

Textural and chemical data for Steinbach help define the crystallization history of the meteorite, including the timing of when different minerals and pyroxene subtypes formed. The lack of significant core-to-rim zoning within individual pyroxene grains suggests an approach to equilibrium, but the overall chemical variability between different pyroxene grains (see the "Phase Chemistry" section), and the apparently continuous variation of compositions for type 2 pyroxene grains (Fig. 6) suggests that pyroxene grains crystallized at different times in an evolving system. The partial enclosure of pyroxene by tridymite (Fig. 2e) implies that tridymite crystallized after pyroxene, but the presence of tridymite inclusions in pyroxene (Fig. 2b) suggests that some tridymite crystallized prior to pyroxene. Thus, the two major silicates could have partially co-crystallized, which is in agreement with previous conclusions (Ulff-Møller et al. 1995; Scott et al. 1996).

Chemical data are consistent with the idea that fractional crystallization was responsible for most of the variation in type 2 grain composition. Positive covariation of most trace

elements with Al (Fig. 6), an incompatible element in pyroxene (Table A2, Appendix), suggests that most trace elements analyzed in pyroxene behaved like incompatible elements. Thus, good evidence for generally incompatible behavior is found for Al, Ca, Cr, V, Y, Dy, Ti, Zr, and Sc, which is consistent with pyroxene-liquid partition coefficients (*D* values) (Table A2). Chromium may have behaved as an incompatible element overall but as a compatible element during the last stages of crystallization, as suggested by the low Cr contents on the rims of many type 2 grains (Figs. 4 and 8). Relatively late crystallization of chromite would account for this behavior in Cr. In contrast to other elements, Mn, Co, and Ni appear to have behaved as largely indifferent or compatible elements during pyroxene crystallization, with *D* values for pyroxene close to 1 (Mn, Co) or greater than 1 (Ni).

The data suggest that clinobronzite, type 1 pyroxene, and depleted type 2 pyroxene all crystallized relatively early, whereas enriched type 2 pyroxene crystallized relatively late. The similar low indigenous abundances of incompatible elements in clinobronzite and type 1 pyroxene (see the "Phase Chemistry" section) are consistent with early crystallization, which is in agreement with textures that imply that both were overgrown by type 2 pyroxene (see the "Textures and Mode" section).

Coarse metal and troilite appear to have formed relatively late. The filling of pyroxene and tridymite grain interstices by metal and troilite (Figs. 1, 2a, and 2d) suggests that metal and troilite flowed between pre-existing silicate grains (Scott et al. 1996). Moreover, coarse metal in Steinbach is crystallographically continuous over distances of at least a few centimeters (Scott et al. 1996). These observations strongly suggest that large metal and troilite grains crystallized from a melt that surrounded pre-existing silicate clusters.

Table 5. LA-ICP-MS data for chromite in Steinbach.[a]

	Mean ± std
Al wt%	3.39 ± 0.01 (3)
Si wt%	0.0812[b] (1)
Ca wt%	n.d.
Sc μg/g	2.31 ± 1.25 (2)
Ti μg/g	1328 ± 28 (3)
V μg/g	3522 ± 87 (3)
Cr wt%	44.76 (3)
Mn wt%	0.629 ± 0.006 (3)
Co μg/g	21.9 ± 4.7 (3)
Ni μg/g	57.2 ± 31.5 (3)
Zn μg/g	5.53 ± 0.29 (3)
Ga μg/g	6.15 ± 0.26 (3)
Rb μg/g	1.02 ± 0.10 (1)
Sr μg/g	2.75[b] (1)
Y μg/g	n.d.
Zr μg/g	2.03 ± 0.20 (3)
Nb μg/g	1.19 ± 0.06 (3)
Cs μg/g	0.378 (1)
Ba μg/g	n.d.
La ng/g	96 (1)
Ce ng/g	43 (1)
Pr ng/g	n.d.
Nd ng/g	57 (1)
Sm ng/g	n.d.
Eu ng/g	35[b] (1)
Gd ng/g	21 (1)
Tb ng/g	n.d.
Dy ng/g	n.d.
Ho ng/g	n.d.
Er ng/g	48 ± 3 (3)
Tm ng/g	16 ± 1 (2)
Yb ng/g	n.d.
Lu ng/g	24 (1)
Hf ng/g	12 ± 4 (2)
Th ng/g	34 (1)
U ng/g	6.8 (1)

[a]std = standard deviation. n.d. = not detected. Values in parentheses refer to the number of analyses averaged. Data are normalized to the average Cr concentration determined by electron microprobe analysis.

[b]Values probably are overestimates and reflect the presence of plagioclase inclusions.

Role of Metamorphism

The composition of pyroxene in Steinbach can be interpreted as largely reflecting igneous processes (see the "Crystallization History" section). However, it is clear that Steinbach cooled very slowly at subsolidus temperatures (see the Introduction), and this may have affected the composition of pyroxene. Specifically, it has been suggested that the abundances in pyroxene of some divalent cations (Ca, Fe, Mg, Mn) were partially homogenized during metamorphism, unlike other elements (Al, Ti, Cr) which were less affected because they diffused more slowly (Ulff-Møller et al. 1995).

We suggest that metamorphism played only a limited role in affecting pyroxene compositions. Although it is true that Mn, Fe, Mg, and Co contents in pyroxene are fairly uniform and that this alone could constitute evidence for metamorphic exchange, the same is not true for Ca, which has notably variable concentrations (see the "Phase Chemistry" section). Thus, any metamorphic redistribution of Ca must have been limited, since it did not destroy the overall chemical variations in Ca between different pyroxene types. In addition, although Fe and Mg contents are more uniform than those of Ca, the tendency for the more incompatible-element-poor type 1 grains to be more enstatitic than type 2 grains (Fig. 3; Table 3) also suggests that any metamorphic equilibration did not completely obliterate primary igneous variations in major elements.

However, Ca is often depleted on the margins of enriched type 2 pyroxene grains (see the "Phase Chemistry" section), and we suggest that this depletion is best explained by subsolidus loss of Ca. There is no reason to expect that this type of rim depletion could be caused by magmatic partitioning, since Ca should have remained highly

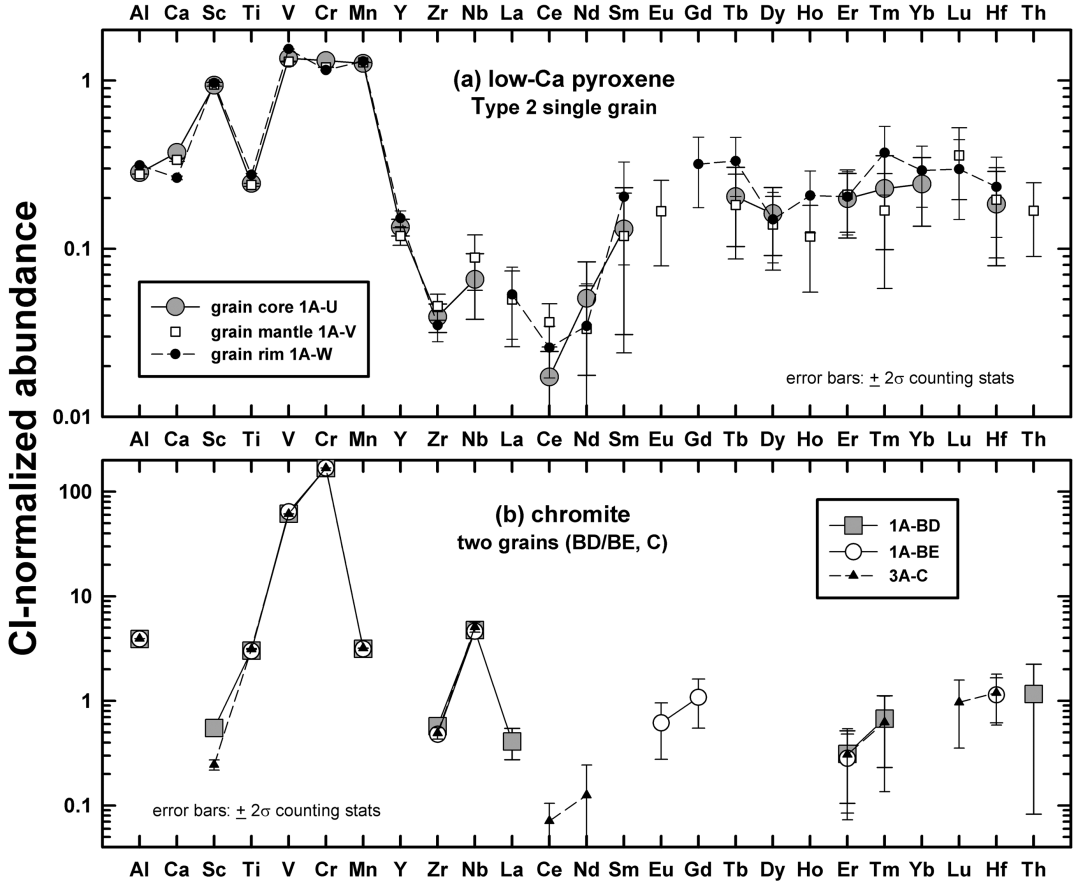

Fig. 5. Elemental abundances obtained with LA-ICP-MS of: (a) a representative single grain of type 2 low-Ca pyroxene (core, mantle, and rim analyses), and (b) chromite (analyses BD and BE in one grain, analysis C in different grain). Error bars indicate ±2σ counting errors. For the individual pyroxene grain, core-rim compositional variations are not apparent except for depletions in Ca and Cr and slight enrichments in Al, Ti, and V towards the grain rim. The data of Anders and Grevesse (1989) were used to normalize compositions to average CI chondrites.

incompatible in low-Ca pyroxene under all magmatic conditions, and since there are no obvious Ca-rich phases in Steinbach that could have served as a sink for this element during co-crystallization with pyroxene. In this regard, the situation for Ca is unlike that for Cr, which is also depleted on the rims of enriched type 2 pyroxene grains (see the "Phase Chemistry" section). Late-crystallizing chromite and a decrease in temperature would both tend to make Cr more compatible during the last stages of crystallization (Barnes 1986), and one or both of these effects was probably responsible for producing Cr depletions on the margins of enriched type 2 pyroxene grains.

Disequilibrium Effects and Early Rapid Cooling

Steinbach silicates show evidence of disequilibrium effects beyond those implied simply by having a range of pyroxene types with different compositions. The most obvious disequilibrium effects are restricted to the first-formed pyroxene, and we infer that such pyroxene crystallized rapidly in contrast to later-formed pyroxene.

The presence of clinobronzite is good evidence for disequilibrium caused by rapid cooling (Reid et al. 1974; Haack et al. 1996). Clinobronzite can be produced from protopyroxene upon quenching, producing the characteristic lamellar and crack structure (Huebner 1980) seen in Steinbach clinobronzite. Although it has been suggested that shock deformation of orthopyroxene produced clinopyroxene lamellae (Wasson et al. 2006), the microstructures of "clinobronzite" are better explained by rapid cooling (Haack et al. 1996) and are analogous to those found for chondrule pyroxene in type 3 and 4 (and less abundantly in type 5) chondrites (Brearley and Jones 1998). In contrast, the predominant "orthopyroxene" (presumably orthobronzite) in Steinbach shows evidence only for slow cooling under subsolidus conditions (Ganguly and Stimpfl 2000).

The chemical similarity between clinobronzite and type 1 grains, together with textural relationships, suggests that both crystallized at a similar stage in melt evolution (see the "Crystallization History" section), so if clinobronzite grains formed by rapid cooling, it is reasonable to suppose that type 1 grains formed under the same conditions. The high

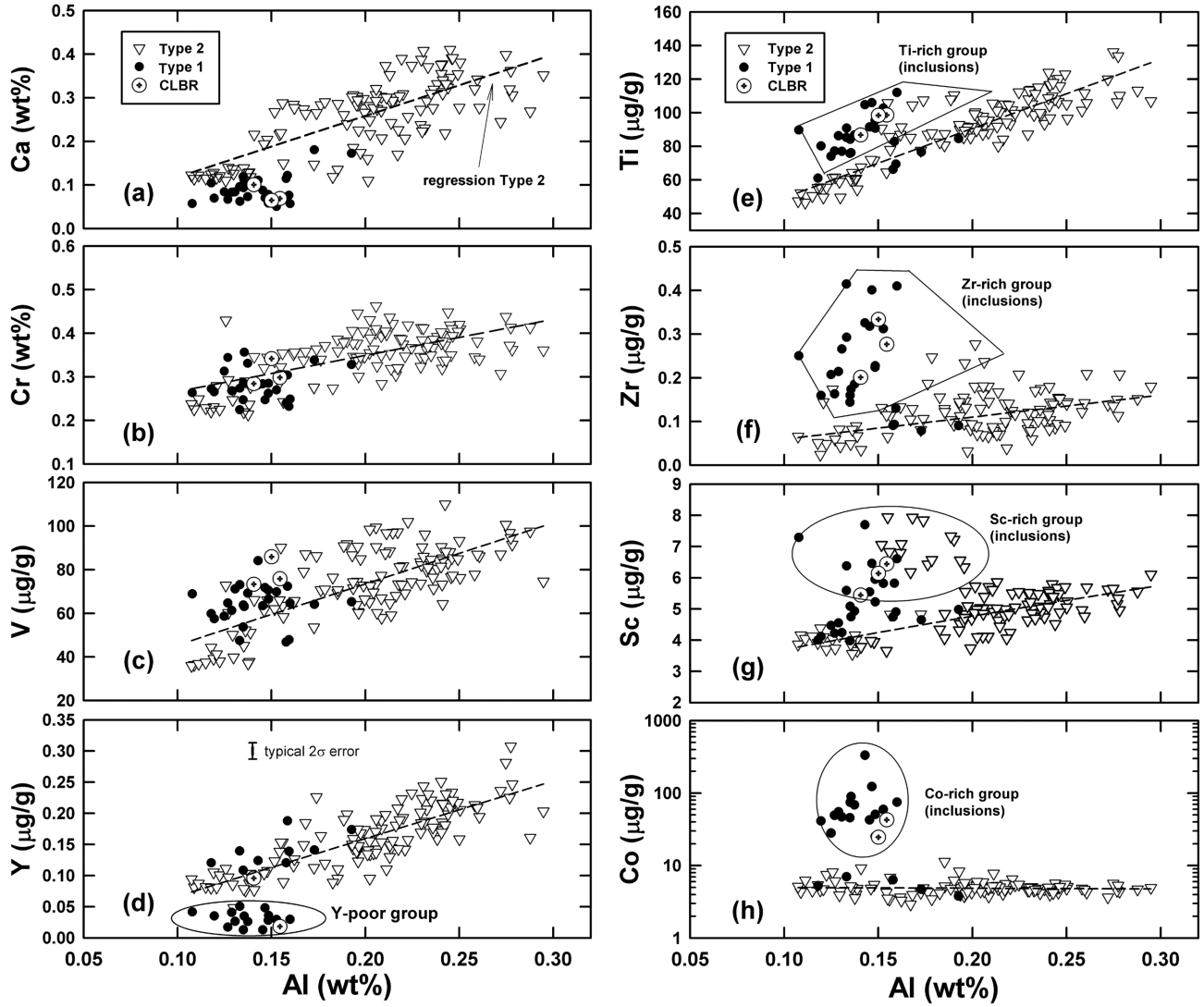

Fig. 6. Aluminum-element covariation diagrams for low-Ca pyroxene illustrating LA-ICP-MS data. Grains are classified as clinobronzite (CLBR), type 1, and type 2 (see text). Large chemical variations are shown by analyses of different type 2 grains; linear regressions are fit through these data. A contamination effect is evident for some analyses caused by the presence of inclusions containing Ti, Zr, Sc, and Co (not necessarily all in the same phase). ±2σ counting errors are indicated by error bars where they exceed the size of the symbols.

density of inclusions in type 1 pyroxene can be explained by preferential early trapping of S-rich melt by this type of pyroxene. Later-crystallizing pyroxene grains and tridymite evidently did not trap as many inclusions. This difference in trapping efficacy could have been caused in part by differences in cooling rate, as rapid cooling would lead to undercooling that could have resulted in rapid growth rates and more opportunity to trap other phases.

The anomalously Y-poor compositions of some pyroxene grains (e.g., Fig. 6d) are also indicative of disequilibrium. There is no obvious textural difference between grains that are Y-poor and those that are not. There are two possible explanations for Y-poor grains, both of which imply disequilibrium: 1) they could be products of disequilibrium crystallization during very rapid cooling, or 2) they could be relict grains that did not crystallize from the same melt as that which produced other pyroxenes. Although neither of the possibilities for producing Y-poor pyroxene can be ruled out, disequilibrium caused by rapid cooling was probably important, as the type 1 grains which mainly populate the Y-poor group probably formed during rapid cooling.

Pyroxene Polytypes

The presence of both clinobronzite and orthobronzite in Steinbach raises the question of why both phases are present. In pyroxene with Wo and Fs values as low as those found in Steinbach (Wo ≤ 1.1 and Fs ≤ 19.4) (Table 2), one would

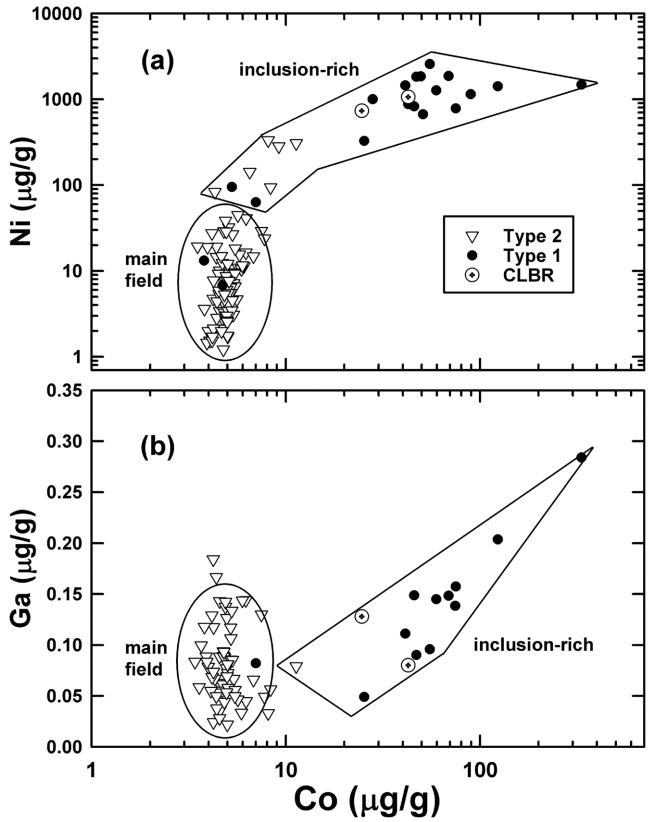

Fig. 7. (a) Co-Ni and (b) Co-Ga variation diagrams for low-Ca pyroxene using LA-ICP-MS data. A trend produced by Ni-Co-rich and Ga-bearing inclusions is shown, together with a "main field" that probably represents indigenous pyroxene compositions.

expect protopyroxene to be the stable polytype present at $T \geq$ 980 °C, and orthopyroxene to be the stable polytype at lower temperatures, based on experiments in pure (Mg-Fe-Ca) systems (Huebner 1980). This implies that only one polytype (protopyroxene) would have been stable at magmatic conditions, which is inconsistent with the presence of both clinobronzite and orthobronzite grains, which presumably crystallized from the same magmatic system.

Phase diagrams based on experiments in pure systems show that orthopyroxene can exist stably with protopyroxene at temperatures as high as ~1445 °C, and that it will be slightly enriched in Wo compared to protopyroxene (Huebner 1980). The more calcic pyroxene in Steinbach could correspond to this orthopyroxene, and the less calcic pyroxenes could correspond to protopyroxene that inverted to clinopyroxene. However, we did not find evidence for the miscibility gap in Wo (or other minor element) content found by earlier workers (Reid et al. 1974; Ulff-Møller et al. 1995) which could otherwise be construed to indicate two polytypes co-existing in equilibrium (Reid et al. 1974). Moreover, there is good evidence that the more calcic type 2 pyroxenes in Steinbach crystallized from a melt more evolved than the less calcic pyroxenes (including both orthobronzite and clinobronzite) (see the "Crystallization History" section) (Ulff-Møller et al. 1995), so there is reason to doubt whether the evolved type 2 and less calcic pyroxenes were ever in equilibrium.

Rather, the data are more consistent with an alternative model in which protopyroxene formed at an early stage of crystallization, and orthobronzite formed at a later stage of crystallization when the melt had evolved past the point at which protopyroxene could exist stably (Ulff-Møller et al. 1995). The composition of the more calcic pyroxene in Steinbach is close to the stability field limit of protopyroxene in pure systems (Huebner 1980), and the addition of minor components would be expected to change phase relationships (e.g., Biggar 1985), raising the distinct possibility that orthobronzite could have become stable and protopyroxene unstable in magmas with more evolved compositions. We suggest that enriched type 2 pyroxene represents primary magmatic orthopyroxene, whereas less calcic clinobronzite and type 1 grains represent pyroxenes that were originally protopyroxene that inverted to clinobronzite or orthobronzite upon cooling. It is unclear whether depleted type 2 grains formed initially under magmatic conditions as protopyroxene or orthobronzite.

Cotectic and Cumulate Origin of Steinbach

We infer that Steinbach ultimately formed on the pyroxene-silica mineral (SiO_2) cotectic as a cumulate, in agreement with the conclusions of Ulff-Møller et al. (1995). A cotectic (or eutectic) origin is suggested by the proportions of pyroxene and tridymite in the meteorite and evidence that some pyroxene and tridymite co-crystallized. Formation as a cumulate is implied based on the chemical variability of pyroxene (see the "Phase Chemistry" section) (Ulff-Møller et al. 1995) and the difficulty in producing the bulk composition of Steinbach by other means.

The pyroxene/(pyroxene + tridymite) weight ratio of Steinbach is relatively well-defined at 0.70–0.75, with a best estimate in this work of ~0.72 (Table 1). In the forsterite-quartz-anorthite system (Andersen 1915), which has precisely determined liquidus relations suitable for quantitative analysis (Morse 1980), this ratio varies along the cotectic from ~0.87 at high temperature on the enstatite-silica join, to ~0.56 at low temperatures where the cotectic joins the pyroxene-silica-anorthite eutectic. Based on this system, Steinbach with pyroxene/(pyroxene + tridymite) ~0.72 corresponds to a cotectic composition where pyroxene and silica would have been in equilibrium with ~12 wt% liquid.

Given the bulk composition of Steinbach, there are two main ways the meteorite could have formed if it originated on the pyroxene-SiO_2 cotectic: 1) it could be a restite produced during partial melting, after feldspathic liquids were removed from the remaining solids; or 2) it could represent a cumulate pile produced during crystallization, with feldspathic liquids removed from the interstices of cumulus crystals. A variant of

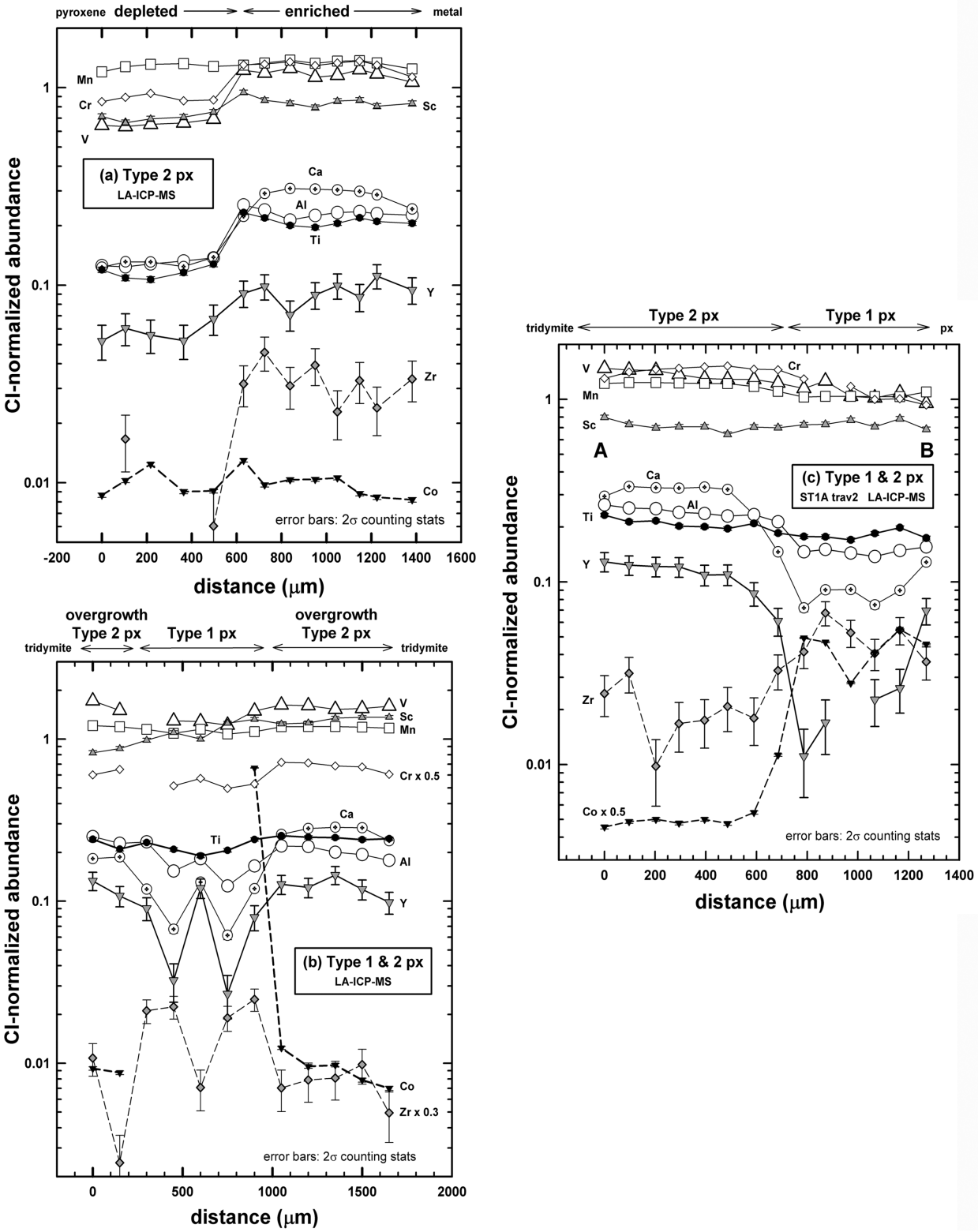

Fig. 8. Chemical profiles obtained by LA-ICP-MS across: (a) composite type 2 pyroxene grains showing enriched and depleted compositions (a portion of a larger pyroxene cluster); (b) a pyroxene cluster containing a type 2 overgrowth around a type 1 core (probably actually two cloudy core regions separated by a narrow type 2 region); and (c) composite type 2 and type 1 pyroxene grains (sample ST1A, traverse 2, a portion of a larger pyroxene cluster shown in Fig. 2e). The data of Anders and Grevesse (1989) were used to normalize compositions to average CI chondrites. Px = pyroxene.

Table 6. The concentration ratio (C_E/C_D) between enriched (E) and depleted (D) type 2 pyroxene and corresponding change in liquid proportion (X) for the fractional crystallization model discussed in the text.[a]

	C_E/C_D	X (%)
Al	2.74	65.2
Ca	3.57	74.4
Sc	1.51	61.2
Ti	2.60	64.6
V	2.25	99.9§
Cr	1.58	60.7
Y	3.31	70.4
Zr	2.67	63.2
Dy	2.25	56.7
Average (omits V)[b]		64.6 ± 5.6

[a] $X = (1 - F)$, calculated from $\log F = (1/[D^{px/liq} - 1]) \times \log (C_E/C_E)$, where $D^{px/liq}$ partitioning values (assumed constant) are given in Table A2, and C_E = concentration in most enriched type 2 pyroxene and C_D = concentration in the most depleted type 2 pyroxene, as defined by linear regression endpoints in Al-element variation diagrams. Elements with well-defined differences in concentration between evolved and depleted type 2 pyroxene are shown. Value after "±" represents the standard deviation.

[b] $X = 63.2\%$ for V and $X_{average} = 64.4 \pm 5.3\%$, if $D^{px/liq}{}_V = 0.19$, as implied by the observed Al-V covariation in Steinbach pyroxene.

the second model is that Steinbach formed as a cumulate, but that feldspathic liquids were lost during melting, as a result of explosive (pyroclastic) activity (Keil and Wilson 1993).

The chemical variability evident for type 2 pyroxene grains provides strong support for the cumulate model. This variability can be explained by a single magma undergoing fractional crystallization (see the "Crystallization History" section). In contrast, if Steinbach was a restite, one would expect little chemical variability in the pyroxene, unless partial melting occurred under highly nonequilibrium conditions. Even if Steinbach was a restite produced under disequilibrium conditions, one would expect individual grains to show more chemical zoning, rather than having generally uniform compositions within individual grains.

Moreover, a restite model for Steinbach requires that the protolith be olivine-poor, in order to generate the overall bulk composition of Steinbach as a pyroxene-SiO_2 residue. An olivine-poor protolith is inconsistent with the ordinary chondrite-like protolith that is likely for Steinbach (see the Introduction), or for any other kind of chondritic protolith except an enstatite chondrite. The latter chondrites have distinctive phase compositions (e.g., nearly pure enstatite, Si-bearing metal), mineral assemblages (e.g., sulfides), and oxygen-isotopic compositions that are unlike what is found in Steinbach, making such a protolith unlikely for the IVA body. Significant processing would be needed to generate an olivine-poor precursor from any olivine-rich chondritic protolith before the melting event occurred to form Steinbach as a restite, requiring an especially complex petrogenesis for the restite model. In contrast, the cumulate model is in some ways simpler, in that possibly suitable precursor melts can be generated by partial melting of an olivine-rich protolith, and that fractional crystallization of such a partial melt can help to create the Si-rich composition of Steinbach.

Crystallization Extent

Presuming that Steinbach formed as a cumulate during fractional crystallization and that chemical variations in pyroxene reflect the evolution of Steinbach magmas (see the "Crystallization History" and "Cotectic and Cumulate Origin of Steinbach" sections), the composition of pyroxene can be used to evaluate the extent of crystallization in the magmas. We used the standard equation for fractional crystallization (e.g., Rollinson 1993) to solve for the amount of crystallization (X) needed to explain the variation in type 2 grain compositions. The model assumes that literature D values for pyroxene (Table A2) were constant during crystallization, and that other phases (including tridymite, chromite, and inclusions in pyroxene) did not chemically affect the melt evolution. It is likely that neither of these assumptions is strictly correct. However, by using data for different elements, one can evaluate whether there is any consistency that would point toward a unique model.

Table 6 shows the degree of crystallization needed to explain the data for those elements that have well-defined differences in average composition between depleted and enriched type 2 pyroxene grains. Table 6 indicates that, with the exception of vanadium, the data are consistent with ~57–74% fractional crystallization between the most incompatible-element-poor and element-rich type 2 pyroxene grains (defined as the endpoint compositions on the regression lines shown in Fig. 6). The literature value for D_V used in models (~0.9) is clearly inconsistent with the data for other elements, and it leads to an unrealistically large amount of crystallization (99.9%). This high value of D_V is incapable of explaining the relatively large difference in composition between type 1 and type 2 pyroxene. The assumed value of D_V for pyroxene is an average of three literature values which themselves show substantial variation (Table A2), making the assumed value uncertain. If instead the value of D_V is estimated based on the data for Steinbach itself, by using the Al-V covariation for type 2 pyroxene (Fig. 6c) and assuming the literature value D_{Al} ~0.04, a value of D_V ~0.19 is obtained. Using this lower value of D_V implies X ~63% based on V, which is consistent with the data for other elements.

If tridymite (or a higher-temperature SiO_2 polymorph) co-crystallized with pyroxene, the appropriate D value to use would be the bulk partition coefficient, rather than the pyroxene-liquid partition coefficient as assumed in Table 6. The concentrations of Al and Ti are similar in tridymite and pyroxene (Table 2), and the same is probably true for the REE (Ulff-Møller et al. 1995) and Y, so the effective D values for

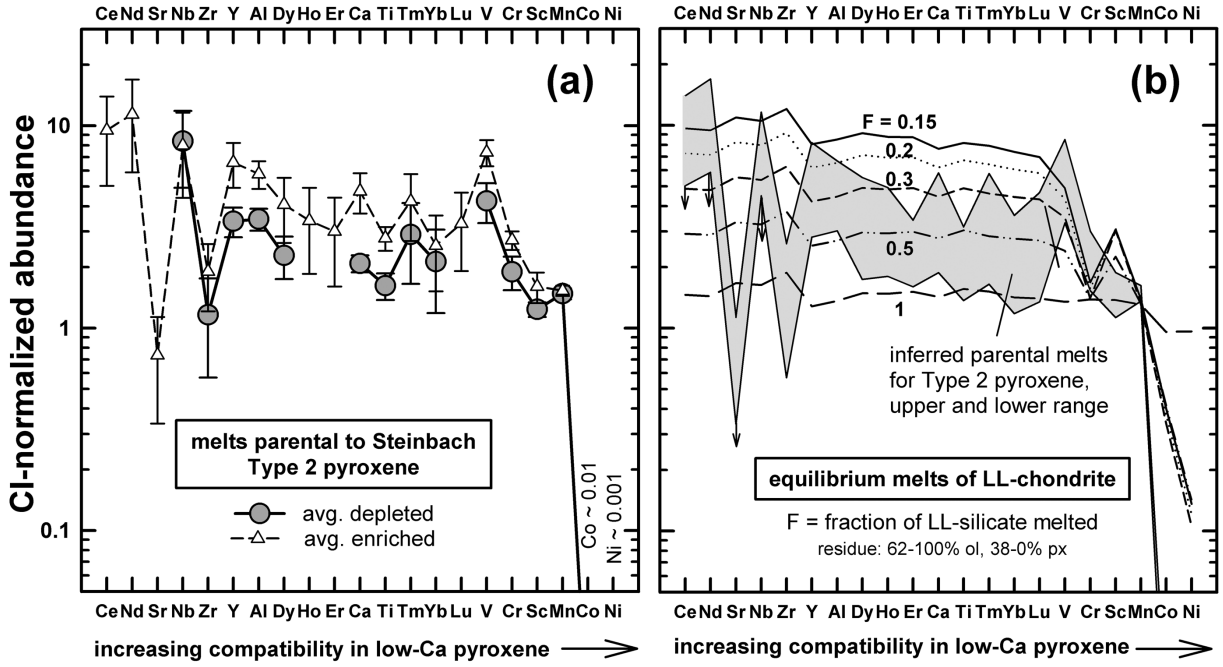

Fig. 9. CI-normalized abundances for parental melt compositions, with elements arranged in order of increasing compatibility in pyroxene. The equilibrium D values from Table A2 were assumed in calculations, except that a value of $D^{px/liq\ V} = 0.19$ was assumed for pyroxene (see text). The data of Anders and Grevesse (1989) were used to normalize compositions to average CI chondrites. a) Inferred melt compositions parental to average depleted and enriched type 2 pyroxene in Steinbach. b) Inferred parental melt composition range from (a) compared to models of equilibrium melts produced by partial melting of an LL chondrite protolith (average LL chondrite composition taken from Lodders and Fegley 1998) at various degrees of partial melting (F = fraction of silicate melt). Downward arrows indicate upper limits on inferred parental melt compositions. The data are best interpreted to indicate that Steinbach parental melts were formed at high degrees of partial melting ($F > 0.3$ and probably ≥ 0.5) (see text).

these elements are probably similar to those assumed in the calculation. However, Ca and Cr concentrations in tridymite are clearly less than in pyroxene (Table 2), and the same could be true for V, so the effective D values of these elements could be less than assumed in the calculation. Thus, the results in Table 6 for Al, Ti, REE, and Y are probably not significantly affected by tridymite crystallization, whereas the results for Ca, Cr, and V could be too low. Omitting the latter three elements yields X ~64 ± 5% (mean and standard deviation), which is about the same as for the larger data set. Thus, there is no evidence that tridymite co-crystallization significantly affected our conclusions based on pyroxene chemistry alone.

It therefore appears that the implied crystallization extent is the same regardless of whether the implied value of D_V for pyroxene is used or whether V data are excluded, and regardless of whether the elements most likely to be affected by tridymite crystallization are excluded or not. We conclude that Steinbach magmas experienced ~60–70% fractional crystallization of pyroxene, with a best estimate of ~64–65%, between the onset and conclusion of type 2 pyroxene crystallization. The internal consistency of this fractional crystallization model for different elements lends strong support to the cumulate origin of Steinbach (see the "Cotectic and Cumulate Origin of Steinbach" section).

Parental Melt Composition

In this section, the compositions of melts in equilibrium with pyroxene are calculated and compared to models of melt compositions produced by partial melting of a chondritic precursor. For calculation of the original melt composition, the least evolved pyroxene compositions (clinobronzite, type 1, depleted type 2) are appropriate, whereas for the final melt composition, evolved type 2 grain compositions are relevant. Figure 9a shows parental melt compositions based on pyroxene data, and Fig. 9b shows the compositions of equilibrium ("batch") melts produced by the partial melting of an LL chondrite–like protolith. Any other type of ordinary or carbonaceous chondrite protolith would give similar results. In all cases except for V, literature D values are assumed. For V, the D value for pyroxene inferred to be applicable during pyroxene crystallization in Steinbach (~0.19) (see the "Crystallization Extent" section) was assumed.

Figure 9a shows that, in general, elements that are more incompatible in pyroxene tend to be more enriched in the parental melt (Fig. 9a). This is most clearly seen for enriched type 2 pyroxenes, which were in equilibrium with parental melt most enriched (~10 ± 5 × CI abundances) in highly incompatible elements (Ce, Nd, Nb), less enriched (~1–2 ×

CI) in slightly incompatible elements (Sc, Mn), and depleted (~0.01–0.001 × CI) in semi-compatible or compatible Co and Ni. A similar tendency is seen for depleted type 2 pyroxene at lower overall abundances. The only significant discrepancies to this pattern are provided by Sr and Zr, which are depleted in the melt compared to other elements of similar incompatibility (Fig. 9a). The discrepancies for these elements are too large to be explained by a factor of ~2 uncertainty in their pyroxene/melt *D* values (using the standard deviations in Table A2 as a measure of uncertainty).

Rather, we suggest that the abundances of Sr and Zr in pyroxene are related to the presence of other phases that appear to contain much of the Zr and Sr budget in Steinbach. Type 1 are enriched relative to type 2 pyroxene grains in Zr by a factor of ~3 (Table 4) as a result of Zr-rich inclusions, possibly ilmenite (see the "LA-ICP-MS Data" section). If these inclusions exsolved from pyroxene, it would have reduced the Zr content in pyroxene and artificially lowered apparent Zr melt concentrations. Alternatively, if the Zr-rich inclusions crystallized early and become trapped within pyroxene, it would have depleted Zr in the melt out of pyroxene crystallized, also leading to artificially low melt concentrations. Similarly, the Sr discrepancy may be caused by the partitioning of this element into another phase, such as plagioclase or tridymite. A small amount of a Sr-rich phase appears to be present in Steinbach in the form of small inclusions, as evidenced by spikes in Sr count rates observed in some LA-ICP-MS analyses of chromite, troilite, and pyroxene. Within pyroxene, evidence of Sr-rich inclusions was found in 8 LA-ICP-MS analyses out of 143 (~5.6%), with 2 analyses (~1.3%) showing clearly coincident spikes in Sr and Ca count rates that are good evidence for plagioclase. Chemical evidence for plagioclase inclusions was also found in chromite.

Figure 9b shows the composition of melts produced by equilibrium melting of an LL chondrite for various melt fractions *F* (0.15–1) compared to the melt composition implied for pyroxene. The melting models assume a simplified restite mineralogy for a chondritic system consisting only of olivine and pyroxene, whose proportions vary depending on extent of melting, with a pyroxene/olivine ratio equivalent to that in LL chondrites at 15% silicate partial melting and decreasing to zero for ≥30% partial melting. These estimates are generally consistent with the pattern of melting in the olivine-anorthite-quartz system (Morse 1980) and with melting experiments on ordinary chondrites (Jurewicz et al. 1995; Feldstein et al. 2001). The actual restite would probably include metal and small amounts of chromite (Feldstein et al. 2001; Jurewicz et al. 1993, 1995), so elements that significantly partition into these phases (e.g., Cr, V, and Nb in chromite, and Co and Ni in metal) could have been partially retained in the source region if these phases were incompletely melted.

The original melt composition would have been similar to the lower range inferred for incompatible elements in Fig. 9b (all elements except for Co and Ni) and the upper range for compatible elements (Co and Ni). Downward arrows are shown for Ce, Nd, and Sr because it is clear that these elements were often below detection limit, so their true lower limit concentrations are less than those shown in the figure. A downward arrow is assigned to Nb in Fig. 9b to indicate that although this element was often positively detected, a large count rate uncertainty exists at the abundances measured (cf. Tables 4 and A1), and actual abundances (especially for depleted type 2 pyroxene) could well have been lower.

For most elements, there is an adequate match between the composition of the inferred original melt and a relatively high degree (F = 0.3–1) of partial melting of the chondritic precursor (Fig. 9b). Melt fractions of F ≥ 0.5 are implied for most REE, Y, Al, Ca, and transition elements such as Ti, Cr, Sc, and Mn. Data for V imply a somewhat lower melt fraction of ~0.3. In contrast, melt compositions inferred from pyroxene data for Co and Ni are over two orders of magnitude less than expected based on this simple melting model (Fig. 9). This is almost certainly because these elements were largely incorporated into co-existing metal and troilite within Steinbach. It seems clear that the low abundance of Sr in Steinbach parental melts as inferred from pyroxene data cannot be attributed to partial retention of this element in plagioclase in the source region, as this would require low (<15%) degrees of partial melting, too low to be consistent with all other elements (Fig. 9b). Instead, the data suggest that Steinbach parental melts formed by ≥30–50% partial melting of an ordinary chondrite-like protolith, with higher degrees of melting (≥50%) being most likely. In any case, olivine would have been the principal, if not only, silicate mineral remaining in the source region.

Redox Effects

Assuming that the similarity in oxygen-isotope compositions between Steinbach and LL chondrites (Wang et al. 2004) is indicative of a LL-like protolith for Steinbach, the chemical composition of its pyroxene implies that it experienced significant FeO reduction (Ulff-Møller et al. 1995; Wasson et al. 2006). The average composition of pyroxene in Steinbach can be used to place constraints on the extent of such reduction regardless of whether it experienced metamorphic homogenization (see the previous section). Although an LL-like protolith is most likely, we also consider the implications of having other types of chondritic precursors.

Figure 10 shows Fe/Mn versus Fe/Mg ratios of type 1 and type 2 pyroxene in Steinbach compared to bulk LL chondrite silicate (Jarosewich 1990), and compared to low-Ca pyroxene in LL4-6 chondrites (Heyse 1979). Average compositions of type 1 and type 2 pyroxenes have overlapping Fe/Mn (within ±1 standard deviation) and differ only slightly in Fe/Mg values (Fig. 10). These average compositions are coincidentally similar to those in H4–6 chondrites (Brearley and Jones 1998).

Compared to the pyroxene in LL chondrites, Steinbach pyroxene has lower Fe/Mn and Fe/Mg and the same Mg/Mn values, implying 37% less FeO (Fig. 10). Although one could interpret this to indicate that Steinbach formed by 37% FeO reduction of an LL precursor, the compositions of silicates in LL4–6 chondrites reflect metamorphic equilibration, whereas for Steinbach, the effects of magmatic processes must be considered.

If the presumed LL protolith were completely molten, the melt would have the composition of bulk LL silicates (assuming partitioning of iron between silicate and nonsilicate fractions at high temperatures identical to that observed in LL chondrites). Based on the experiments of Kennedy et al. (1993), which indicate equilibrium values of $K_D^{Fe/Mn} = 0.976$ and $K_D^{Fe/Mg} = 0.28$ (both on mass basis), low-Ca pyroxene in equilibrium with melt would have only slightly lower Fe/Mn and significantly lower Fe/Mg values than the melt (shown by "equilibrium px" in Fig. 10). It is the composition of this equilibrium pyroxene that should be compared to that in Steinbach. To create a suitable precursor melt for Steinbach that could have crystallized pyroxene assuming the same K_D values as given above, ~56% FeO loss is required from a LL-silicate total melt (Fig. 10).

Roughly the same amount of FeO-loss would be required if the LL protolith was incompletely molten. For partial (as opposed to total) melting (see the "Parental Melt Composition" section), one would expect both the melt and pyroxene in equilibrium with it to have more FeO-rich compositions, but with essentially the same K_D relationship as before. This implies that the pyroxene in equilibrium with the partial melt would have had a composition located somewhere on the "igneous fractionation" line in Fig. 10. Because $K_D^{Fe/Mn}$ is close to 1, Fe/Mn values in the melt are not very sensitive to the amount of melting, and so can be used to constrain the amount of reduction. Although less eventual pyroxene crystallization would be needed to make Steinbach from a partial melt, essentially the same amount of FeO reduction (~53–55%) would be required as for a total melt (~56%), using Fe/Mn as the principal criterion.

The same type of reasoning can be used to infer the extent of reduction with other potential chondritic protoliths (excluding once again the enstatite chondrites for the reasons given in the "Cotectic and Cumulate Origin of Steinbach" section). Assuming the chemical data of Jarosewich (1990), the corresponding values for L and H chondrite protoliths would be ~45–46% and 30–31% FeO loss, respectively. For a more oxidized carbonaceous chondrite–like precursor, the required FeO loss would exceed that required for LL chondrites (>56%).

Thus, if Steinbach formed by partial-to-complete melting of an ordinary or carbonaceous chondrite protolith, substantial FeO reduction would have had to occur. Most likely, such widespread reduction occurred in the silicate melt out of which pyroxene crystallized, as there is little evidence for this process occurring on a large scale after or during pyroxene crystallization. During FeO reduction, oxygen would have been evolved by reaction and additional Fe-metal formed.

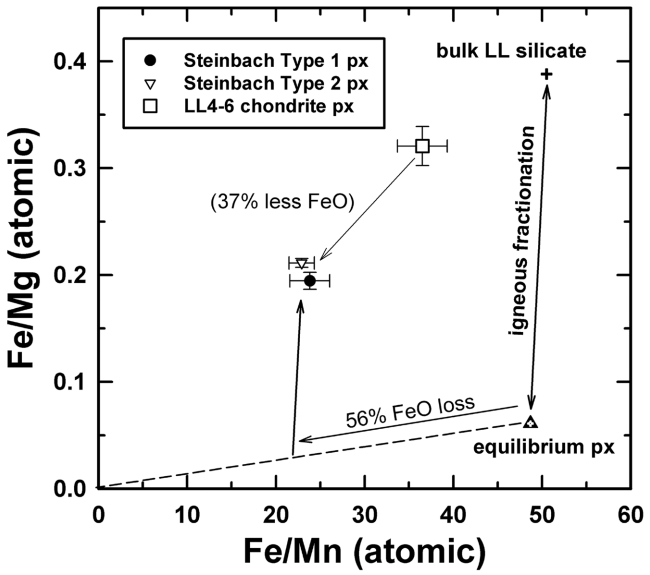

Fig. 10. Fe/Mg and Fe/Mn ratios for average low-Ca pyroxene in Steinbach (average type 1 and 2 compositions from Table 3) compared to that in LL4–6 chondrites (Heyse 1979), and bulk LL chondrite silicate (Jarosewich 1990). Low-Ca pyroxene in equilibrium with a melt of bulk LL chondrite silicate would have the composition indicated by "equilibrium px" based on equilibrium partitioning data of Kennedy et al. (1993). To produce the composition of Steinbach pyroxene implies 56% FeO loss (see text).

An independent analysis recently led Wasson et al. (2006) to argue for significant FeO and FeS reduction in the formation of the IVA parent body, based on the inferred composition of IVA metal prior to fractional crystallization. Assuming a protolith composed of two-thirds L and one-third LL materials, they estimated iron reduction involving loss of ~22% FeO and ~37% FeS to create the additional Fe metal necessary to explain the Ni content of IVA metal. Although this amount of FeO reduction is less than what we estimate based on pyroxene composition for a comparable protolith, it is significant that the compositions of both the silicate and metal fractions in IVA meteorites are consistent with large-scale reduction.

Petrogenesis of the Silicate Fraction in IVA Stony Irons

We use the constraints outlined in the preceding sections together with phase diagrams to describe an overall model applicable to the silicates in IVA stony irons (Steinbach and São João Nepomuceno). Figure 11 shows two variants of olivine-plagioclase-quartz phase liquidus diagrams that are useful, including a projection onto the olivine-plagioclase-quartz plane from wollastonite and orthoclase (Fig. 11a) (Longhi 1991), and the forsterite-anorthite-quartz system

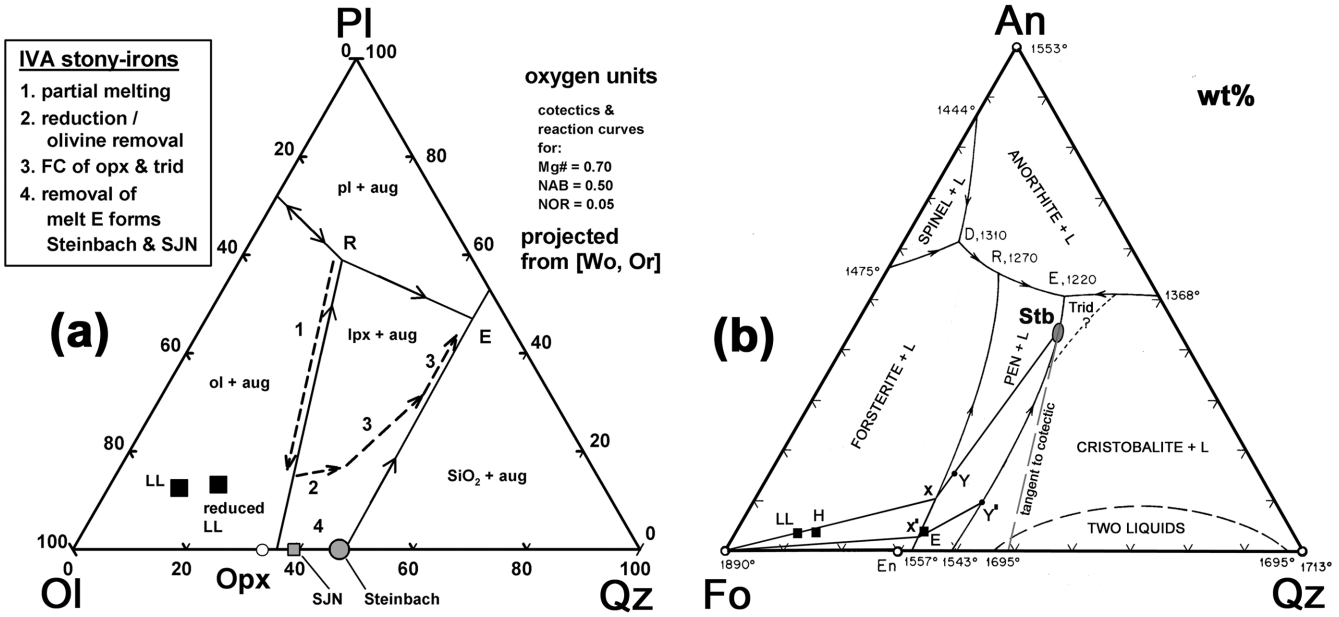

Fig. 11. Two variants of olivine-plagioclase-quartz phase liquidus diagrams that are useful for understanding the petrogenesis of IVA stony irons. a) Projection onto the olivine-plagioclase-quartz plane from wollastonite and orthoclase (Longhi 1991; algorithm given in Ruzicka et al. 1999), showing the inferred chemical evolution of IVA silicate magmas, the effect of the implied FeO reduction on LL chondrite magmas, and the bulk compositions of Steinbach (this work) and São João Nepomuceno (SJN-Scott et al. 1996). Ol = olivine, pl = plagioclase, qz = quartz, aug = augite, lpx = low-Ca pyroxene, and R is a peritectic and E the eutectic. b) The forsterite-anorthite-quartz system (Morse 1980), showing the inferred solidification composition of Steinbach (Stb), the liquid composition path limits x-Y-Stb and x′-Y′-Stb in Steinbach, and the average composition of LL, H, and E chondrites (LL, H, and E, respectively) (Jarosewich 1990). Fo = forsterite, An = anorthite, Qz = quartz, En = enstatite, PEN = protoenstatite, Trid = tridymite, L = liquid. Temperatures are in degrees Celsius. R and E as in part (a). See text.

(Fig. 11b) (Morse 1980). The latter diagram has precisely determined phase boundaries more useful for quantitative analysis, whereas the former has a more complex composition probably more relevant for natural systems. We also interpolated temperatures between the olivine-anorthite-quartz system with Mg# = Mg/(Mg + Fe) atomic = 0.59 and Mg# = 1.0 (Morse 1980) to obtain estimates of temperatures most suitable for the composition of Steinbach and São João Nepomuceno (hereafter SJN) with Mg# ≥ 0.8.

Figure 11a shows the model proposed for the stony-iron IVAs, assuming a cumulate origin for Steinbach with late loss of feldspathic liquids (see the "Cotectic and Cumulate Origin of Steinbach" section). It involves the following steps: 1) extensive partial melting of an ordinary chondrite protolith (see the "Parental Melt Composition" section), driving the composition of the liquid from peritectic composition R up the olivine-pyroxene reaction boundary with increasing degrees of melting; 2) FeO reduction of the silicate liquid (see the "Redox Effects" section) accompanied by olivine removal, moving the composition of liquids well into the low-Ca pyroxene crystallization field; 3) extensive fractional crystallization of pyroxene from the liquid (see the "Crystallization Extent" section), ultimately finishing with cotectic crystallization of pyroxene and tridymite (see the "Cotectic and Cumulate Origin of Steinbach" section); and finally, 4) removal of residual feldspathic liquids from the cumulus pile (see the "Cotectic and Cumulate Origin of Steinbach" section) to form the present composition of Steinbach and SJN (Fig. 11a). This overall model agrees with the analysis of Ulff-Møller et al. (1995), but our study provides additional constraints on each of these steps.

The initial parental liquids out of which Steinbach crystallized were probably produced by ≥50% silicate partial melting of an ordinary chondrite protolith (see the "Parental Melt Composition" section). The melt composition would be constrained in equilibrium to lie along the olivine-pyroxene reaction boundary if all plagioclase melted and at least trace amounts of pyroxene were present. The likely melt composition for Steinbach would have been between the limiting points of x and x′ in Fig. 11b, found by extrapolating the Y-Stb and Y′-Stb trajectories (discussed below) toward En. Figure 11b shows that these limiting compositions can be obtained by the removal of forsterite from the average LL, H, or any ordinary chondrite composition. A carbonaceous or R chondrite protolith would also be viable, provided the amount of FeO reduction were larger (see below). Even an enstatite chondrite–like starting composition would be consistent with the parental melt (black dot next to an E in Fig. 11b), although we do not believe this protolith to be realistic for the IVAs (see the "Cotectic and Cumulate Origin of Steinbach"

section). In other words, separation of olivine from any plausible chondritic protolith at large degrees of partial melting can produce the implied melt compositions. At melt compositions x and x′, the system would consist almost exclusively of silicate liquid and olivine, with only a trace amount of pyroxene. Essentially the same thing is suggested by other data for Steinbach: models suggest high degrees of partial melting in which little if any pyroxene was unmelted (see the "Parental Melt Composition" section), and chemical data for pyroxene imply that virtually all of the pyroxene in Steinbach could have crystallized from a melt, with only a small quantity of especially yttrium-poor pyroxene possibly being relict and unmelted (see the "Disequilibrium Effects and Early Rapid Cooling" section). The temperatures corresponding to points x and x′ in Fig. 11b correspond to ~1450 °C and ~1490 °C, respectively, for an Mg# = 0.8 system. We suggest this temperature of ~1450–1490 °C was the true maximum reached by Steinbach. For SJN, the initial melt composition would probably have been closer to x′ than x, and the maximum temperature closer to ~1490 °C.

For comparison, a liquidus temperature of ~1350–1400 °C for Steinbach was inferred by previous workers based on the pattern of Al-Cr covariation in pyroxene and the temperature dependence of the pyroxene/melt partition coefficient D_{Cr} (Ulff-Møller et al. 1995). Using our larger data set for pyroxene and the same approach as used by Ulff-Møller et al. (1995), we estimate D_{Cr} ~0.51. Together with the data of Barnes (1986), this implies T ~1450 °C, which should correspond to an interval between depleted and enriched type 2 pyroxene. This must be less than the maximum temperature, but it is already higher than the liquidus temperature estimated by Ulff-Møller et al. (1995). Thus, our estimate of the maximum temperature experienced by Steinbach (1450–1490 °C) is in better agreement with our implied value of D_{Cr}. It seems clear that the maximum temperature for Steinbach silicates must have exceeded 1450 °C, and easily could have been as high as 1490 °C. The latter value is similar to the maximum temperature estimated by Wasson et al. (2006) for the onset of metal crystallization in IVA irons (1497 °C) based on metal compositions.

Olivine must have separated from an ordinary (or carbonaceous or R) chondrite–like composition to create Si-rich liquids that could crystallize to form IVA silicates (Ulff-Møller et al. 1995). Removal of olivine would drive the bulk composition of the system away from olivine and into the low-Ca pyroxene primary crystallization field (Fig. 11). In order to create Si-oversaturated liquid compositions ending on the pyroxene-silica cotectic, however, one has to do more than remove unmelted olivine; one must also convert some normative olivine in the liquid to normative quartz (Ulff-Møller et al. 1995). In terms of Fig. 11b, one has to "close the gap" in liquid compositions between x and Y or between x′ and Y′. This can be accomplished in one of two ways: either by additional fractional crystallization of pyroxene after olivine removal or by FeO reduction. Either of these processes seems reasonable since there is evidence for reduction (see the "Redox Effects" section), and not all of the early crystallizing pyroxene may have been preserved in Steinbach. However, at least some FeO reduction was necessary if the protolith were an ordinary chondrite (see the "Redox Effects" section). Figure 11a shows the effect of the implied FeO reduction process on bulk LL silicate. This shift is sufficiently large to create the needed Si-oversaturated liquid, provided that the reduction process occurred at relatively high temperatures, when the liquid was close to its most quartz-normative-rich composition on the reaction boundary (i.e., between x and x′ in Fig. 11b). Thus, based on the topology of the phase diagram itself, we conclude that FeO reduction probably occurred when the temperature was highest.

In Steinbach, the final composition was attained after ~65% fractional crystallization of pyroxene (see the "Crystallization Extent" section). In Fig. 11b, two limiting trajectories for the liquid composition during this fractional crystallization step are shown, Y-Stb and Y′-Stb. The bulk composition reached by Steinbach (Stb in Fig. 11b) is found by drawing a tangent to the pyroxene-silica cotectic, which has the same En/(En + Qz) ratio as the pyroxene/(pyroxene + tridymite) ratio (~0.72) in the meteorite (see the "Cotectic and Cumulate Origin of Steinbach" section). Trajectory Y-Stb assumes the limiting condition of 65% fractional crystallization involving pyroxene only, with tridymite joining the crystallization sequence only at the very end when the cotectic was reached. Trajectory Y′-Stb assumes the other limiting condition in which 65% fractional crystallization of pyroxene is accompanied at all times by co-crystallization of tridymite. The actual liquid trajectory was between these two limiting cases. Although the fractional crystallization trajectory taken by SJN is not well constrained, we suggest that SJN liquids may have evolved closer to composition Y′ than Y in Fig. 10b, as removal of a residual liquid from Y′ would be more consistent with cotectic crystallization to produce the pyroxene-rich SJN composition. Less pyroxene crystallization is implied for SJN than for Steinbach.

At the final composition attained by Steinbach (Stb in Fig. 11b), the silicate fraction would consist of both pyroxene and tridymite in the observed proportions, as well as ~12 wt% liquid. This bulk composition corresponds to a temperature of ~1240 °C in the olivine-anorthite-quartz system with Mg# = 0.8. At this temperature, the most incompatible-rich type 2 pyroxenes would have finished crystallizing, and the residual liquid must have been lost from the system. This residual liquid could have been pushed out during formation of the cumulus pile, perhaps by solidification of metal (Scott et al. 1996). We suggest that a similar process occurred to form SJN, but the higher pyroxene/(pyroxene + tridymite) ratio in SJN (~0.91 wt%) (Scott et al. 1996) implies that it formed on a different position on the cotectic, closer to the

pyroxene-silica join. An SJN-like pyroxene/(pyroxene + tridymite) ratio is obtained along the cotectic close to the pyroxene-SiO_2 join for Mg# ~0.8.

It is conceivable, albeit unlikely, that the stony irons were produced by a variant of the model described above, involving the loss of feldspathic liquids early rather than late (see the "Cotectic and Cumulate Origin of Steinbach" section). The petrogenetic steps would remain largely the same, except that removal of feldspathic liquids would occur first during partial melting. Removal of the first peritectic melt (*R*) would drive the composition of the residual solids to the olivine-pyroxene join (Fig. 11). The resulting olivine-pyroxene mixture would need to be partly melted, with the liquids FeO-reduced and fractionally crystallized as before. Steinbach and SJN could still represent cumulates in this scenario, but the temperatures needed to generate the parental melts would have been higher, at least as high as the olivine-pyroxene peritectic or eutectic (>1505 °C for Mg# ~0.8), but probably much higher (~1600–1700 °C) in order to generate a significant proportion of melt.

Early loss of feldspathic melt is much less likely than late removal. To form the stony irons by the early loss model would probably require two melting events because of the different temperatures involved during melting: one to remove the feldspathic liquids, and a second at a much higher temperature to melt the olivine-pyroxene residue. The second melting would be difficult to achieve with short-lived ^{26}Al, as this element will concentrate in the first-formed melt and be removed from the system. Even if ^{26}Al decay was not responsible for melting, there is no evidence that it or other incompatible elements were removed in an early partial melt. Indeed, the relatively uniform and slightly superchondritic abundances of incompatible elements inferred for the initial parental melt in Steinbach (see the "Parental Melt Composition" section) argues strongly against the early loss scenario.

Whether or not the proposed model for stony-iron IVAs is also strictly applicable to the other silicate-bearing IVAs is unclear, but obviously the processes involved in forming Gibeon and Bishop Canyon cannot have been identical to the stony irons, as they have drastically different textures and mineral abundances (Scott et al. 1996), as well as different compositions for tridymite (Ulff-Møller et al. 1995). The only way to create pure SiO_2 in Gibeon and Bishop Canyon with the model suggested for the stony irons is for all pyroxene to be removed, either by extensive FeO reduction (Ulff-Møller et al. 1995), or by a mechanical process involving differential movement between pyroxene and silica minerals. Although neither possibility can be ruled out, it is difficult to imagine a sufficient driving force for the extensive reduction that would be needed (Scott et al. 1996). We concur with Wasson et al. (2006) that silica minerals in Gibeon and Bishop Canyon probably formed by injection of silica into veins; this would be consistent in these meteorites with the plate-like morphology of the silica, which tends to occur at metal grain boundaries. Wasson and coworkers suggested deposition of silica from a vapor; we consider crystallization from a melt as also possible.

Implications for the IVA Parent Body

The petrologic model for IVA stony irons (see the previous section) has significant implications for the evolution of the IVA meteorite parent body. For example, at the maximum temperatures implied for the silicates in Steinbach (1450–1490 °C), the metal-sulfide system of an ordinary chondrite would be largely molten (e.g., Hsieh et al. 1987; Kubaschewski 1982). Thus, partial melting to the extent implied by Steinbach silicates should have produced a parent body consisting mainly of metallic liquid, silicate liquid, and solid olivine. Moreover, the IVA stony irons are best explained as having formed by the incorporation of cumulus silicate minerals within a metallic melt after a significant amount of fractional crystallization (see the "Crystallization History," "Cotectic and Cumulate Origin of Steinbach," and "Crystallization Extent" sections).

The three models previously proposed that seem most viable for IVAs are 1) the injection of silicate liquid into a partially molten core (Ulff-Møller et al. 1995); 2) collisional break-up and reassembly (Haack et al. 1996); and 3) two impacts, involving melting of metal and silicate in separate impact events (Wasson et al. 2006). However, we consider these models as originally proposed to be problematic for a variety of reasons. In the injection model, silicate liquid is drawn into a partially molten core, most likely by solidification shrinkage of core (Ulff-Møller et al. 1995). However, this model cannot explain in any obvious fashion the evidence for rapid cooling of silicates at high temperatures, the variable metallographic cooling rates inferred for metal in different IVA irons and stony irons, nor the apparent correlation of metallographic cooling rates with the composition of metal (see Introduction). Moreover, one cannot have significant solidification shrinkage of the core if it was nearly fully molten at the high temperatures we infer. In the collisional break-up and reassembly model, a largely solidified object is catastrophically fragmented and re-accreted, with the re-accreted material consisting largely of solid metal and silicate fragments (Hacck et al. 1996; Scott et al. 1996). This model cannot easily explain the correlation of metallographic cooling rates with metal composition. Similarly, it cannot explain the high temperatures inferred for silicate melt if the reassembled object consisted largely of solid fragments. It also cannot explain metal-silicate textures in the stony irons, which imply that metal was molten and that this metal entrained pre-existing cumulus silicates. Finally, the two-impact model envisions a first shock event that creates metallic melt beneath an impact crater, which then drains to the center of the parent body and solidifies into a

core, followed by second shock event that partly melts overlying silicates and injects them as a liquid-crystal mush into the solid core (Wasson et al. 2006). This model also cannot easily explain the correlation of metallographic cooling rates with metal composition, nor the strong textural evidence that metal was largely molten when silicates crystallized.

We suggest that a new model, involving simultaneous endogenic heating and collisional disruption, can best explain the data for IVA meteorites. This model is illustrated schematically in Fig. 12. A major impact collision occurs when the IVA progenitor was substantially molten. As a result of the comparable sizes of impacting bodies and the relatively low escape velocity of the IVA progenitor compared to the impact velocity, the progenitor is extensively disrupted, and only a portion of the original body re-accretes or remains. This secondary body, the immediate parent body of IVA meteorites, is largely molten, rich in metal, and solidifies from the outside in. In Fig. 12, we show the IVA progenitor as a larger "target" colliding with a smaller "impactor." However, the IVA progenitor could equally well have been the smaller body. Indeed, smaller bodies are better candidates for major disruption events during collisions owing to their lower escape velocities (Asphaug et al. 2006). Asphaug and coworkers (2006) showed examples of model collisions in which the mantles of impactors are effectively removed to expose metal cores and suggested that this process could have been important for producing iron meteorite parent bodies. This mechanism may be specifically relevant for IVA meteorites.

Prior to impact, we suggest that the progenitor was partly molten as a result of endogenic heating, probably as a result of decay of short-lived radionuclides (e.g., Baker et al. 2005; Bizzarro et al. 2005; McCoy et al. 2006; Ghosh et al. 2006; Wadwha et al. 2006). In the case of the IVAs, such internal heating could have raised the temperature to 1450–1490 °C, the maximum temperature we infer for Steinbach. In Fig. 12, the progenitor IVA body is portrayed as having a liquid metallic core. This reflects calculations which suggest that on a relatively small (e.g., 400 km diameter) body, gravity-driven flow of metallic liquid through pores between unmelted silicate grains will occur rapidly (only ~3 yr to traverse the radius of the body, assuming a grain size of 2 mm, a melt fraction of 0.5, a viscosity of liquid metal of 4×10^{-3} Pa-s [Lide 1990], and a density difference between liquid metal and solid silicate of 3.5 g/cm^3). More viscous silicate liquids will take much longer to traverse the same distance (~24,000 years, assuming a viscosity for silicate liquid of 10 Pa-s [Turcotte and Schubert 1982] and a density difference of 0.5 g/cm^3 between solid and liquid silicate).

We ascribe to the impact disruption event three processes that are inferred to have occurred in the IVA stony irons at high temperatures: separation of liquids from olivine (see the "Petrogenesis of the Silicate Fraction in IVA Stony Irons" section), FeO reduction of liquids (see the "Redox Effects"

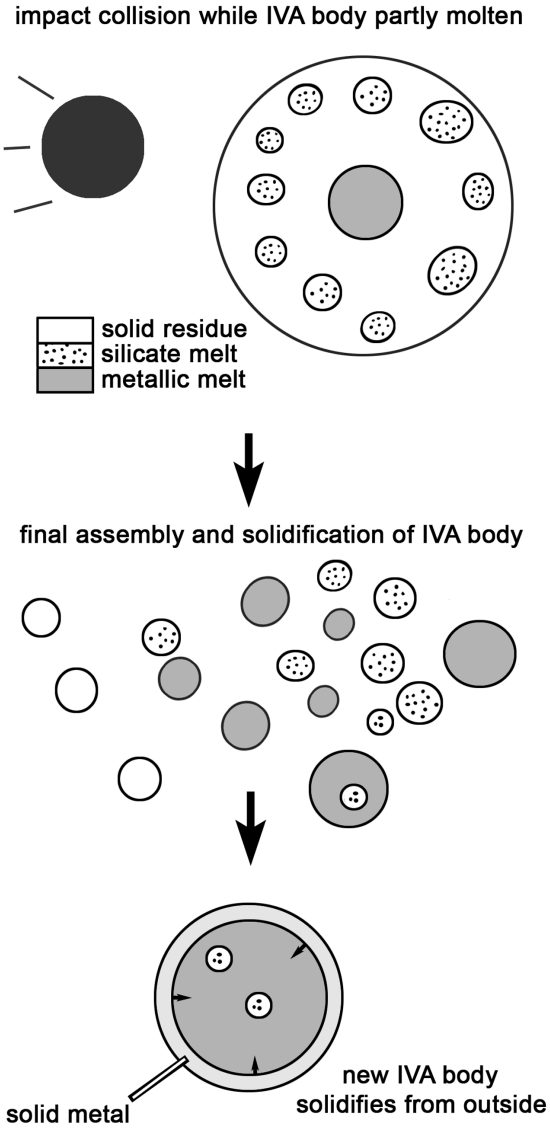

Fig. 12. An illustration showing the proposed evolution of the IVA parent body. See text.

and "Petrogenesis of the Silicate Fraction in IVA Stony Irons" sections), and rapid cooling initially (see the "Disequilibrium Effects and Early Rapid Cooling" section). To this list can be added loss of volatile major (e.g., S) and trace elements (Ga, Ge), caused by vaporization and venting of gas to space (Wasson et al. 2006). Impact disruption provides a mechanism to explain all of these processes at high temperatures, which are otherwise difficult to explain simultaneously.

For the IVA body, we suggest that an impact collision provided a means to remove an olivine-rich mantle, as well as to inject silicate melt into liquid core materials. Removal of an overlying mantle from a core is a plausible outcome during

collisions (Asphaug et al. 2006). In addition, there is experimental evidence that liquids will move more rapidly than solids during the passage of a shock wave. For example, in a Hugoniot state for a shock wave moving at ~5–6 km/s, molten komatiite (Miller et al. 1991), molten fayalite (Chen et al. 2003), and molten diopside and molten anorthite (Rigdin et al. 1989) travel at speeds of ~1.2–1.6 km/s, whereas solid dunite (Dick et al. 1973), solid fayalite (Chen et al. 2003), and pure hot γ iron (taenite) (Chen et al. 2004) travel at speeds of ~0.2–0.65 km/s. This suggests that there is a fundamental difference between how liquids and solids respond to hypervelocity impacts. It is thus reasonable to suppose that impacts could lead to a solid-liquid fractionation.

During the impact event, FeO reduction could have occurred in silicate liquid to generate more metal and to bring silicate liquids into the pyroxene stability field. Significant FeO reduction (ranging up to almost complete loss of FeO at the highest shock pressures) has been observed in experimentally shocked basalt liquids (Rowan and Ahrens 1994). Thermal decomposition of FeO and other volatile species would be expected to occur as a result of the transient high temperatures involved in a shock event (Wasson et al. 2006), especially if hot FeO-bearing liquids were decompressed and exposed to space, where they would be expected to boil. Reduction of iron may also have been aided if C were present (Wasson et al. 2006).

Relatively rapid cooling would have occurred at the time of disruption if the liquids were exposed to space, accounting for the presence of clinobronzite, type 1 pyroxene, and the possible retention of minor relict pyroxene. Haack et al. (1996) modeled collisional disruption of the IVA body and suggested that a cooling rate sufficiently high to form clinobronzite (~100 °C/h) could be obtained at 1200 °C. We note that the presence of clinobronzite and the inferred presence of protopyroxene does not place strict constraints on the temperature at which rapid cooling occurred, only that it be in excess of ~980 °C (see the "Pyroxene Polytypes" and "Disequilibrium Effects and Early Rapid Cooling" sections). For example, cooling rates could have been high at $T >$ 1240 °C, and much slower at $T \sim$1240 °C, the temperature at which Steinbach silicates had finished crystallizing (see the "Petrogenesis of the Silicate Fraction in IVA Stony Irons" section).

If the parent body was substantially molten originally, one would expect the same to be true for the secondary body that re-assembled after or survived the impact. According to Haack et al. (1996), a parent body disruption event would entail only minor heat loss, as the disruption and reassembly process would have been fairly rapid, and as opacity from the debris cloud would have thermally insulated the disrupted materials. A second-generation liquid body would be expected to cool from the outside and to undergo vigorous convection initially. Silicate pods (perhaps formed by liquid immiscibility) entrained in the metal would have convected together with it. As convection slowed and eventually stopped, solidification should have begun at the surface and moved inward. If silicate liquids were concentrated in discrete pods, it would be possible to keep together in one place pyroxene that crystallized over an extended temperature interval. Meanwhile, progressively more Ni-rich metal would crystallize toward the center of the body. Wasson et al. (2006) modeled Steinbach metal as having formed by ~77% fractional crystallization, which is in good agreement with the ~65% fractional crystallization we estimate for the silicate (considering that solidus temperatures are lower for S-bearing metallic melt), supporting the idea that both crystallized together as part of the same process.

Ultimately, the body would completely solidify, with the interior cooling by conduction. Goldstein and colleagues have modeled the latter process and suggest that a metallic body 300 km in diameter would cool at rates comparable to those inferred by metallographic techniques for IVA meteorites, more rapidly near the surface (~7000 °C/Myr) and slower toward the center (~90 °C/Myr) (Yang et al. 2006, Forthcoming). Unlike other models, this scenario of a solidifying metallic core stripped bare of its mantle can explain the observed Ni-cooling rate correlation. To maintain the correlation requires that significant convection could not have occurred below the temperature at which metal crystallized.

The major problem with any model for the IVA stony irons is that it is unclear how silicate and metallic liquids of very different density could co-exist, since buoyancy effects should have caused the two to separate. For example, assuming Stokes Law, Ulff-Møller et al. (1995) calculated that silicate spheres with a radius of 1 cm and a density of 3 g/cm^3 situated 200 m from the center of an entirely liquid core (radius = 2 km, density = 7.5 g/cm^3) would rise to the surface of the metal in about 15 hours. We suggest one or more of the following possibilities to decrease Stokes velocities or hinder metal-silicate separation: 1) dynamic forces (e.g., convection) to keep silicate and metallic liquids from separating; 2) rapid cooling rates at high temperature to minimize the effect of having low-viscosity fluids present initially; 3) partial crystallization to dramatically increase the effective viscosities of the liquids, and to hinder vertical movement of material; and 4) neutralization of buoyancy effects after the onset of crystallization, by the attachment of solid metal to solid silicate, a variant of the dendrite foundering model of Ulff-Møller et al. (1995). It is beyond the scope of this paper to evaluate all these processes. However, we note that if cooling rates were as rapid as the ~100 °C/h implied for clinobronzite, the solidification time scale would be rapid compared to the time scale for metal-silicate separation by Stokes's Law. Even a body that was completely molten initially would soon partially solidify, hindering the upward rise of buoyant materials. In any case, although it is

difficult to be sure of the exact reason why metal and silicate liquids did not completely separate, the evidence is strong in the IVAs that some way was indeed found.

Another consideration that bears on the origin of the IVAs is the low proportion of IVA stony irons (2 identified members) compared to irons (over 50 identified members) (Scott et al. 1996). In the case of a model involving collisional disruption and reassembly of a largely molten body, one would expect much more silicate liquid to be produced than metallic liquid, if the original protolith was chondritic. To explain the dearth of stony-iron IVAs by this model requires either that 1) silicate-bearing IVAs were preferentially destroyed, or that 2) the final liquid body contained mostly metallic liquid. Preferential destruction of silicate-bearing IVAs could have occurred by smaller impact events, either on the parent body or while meteoroids were in interplanetary transit. The long (~450 Myr) exposure age of 8 of 10 IVA irons (Voshage and Feldman 1979) suggests ample time for destruction of mechanically weak, silicate-rich meteoroids; the similar ages support the idea that all IVAs were derived from a single parent body. It is also possible that the disruptive impact event that produced the final liquid body may have mechanically separated not only liquid from solid olivine, but also metallic and silicate liquid from each other.

CONCLUSIONS

The silicate fraction of the Steinbach stony-iron meteorite probably solidified at ~1240 °C on the pyroxene-silica mineral (SiO_2) cotectic as a cumulate after residual feldspathic liquids were pushed out of the cumulus pile. Textural data imply that coarse metal and troilite grains crystallized from a melt that surrounded pre-existing silicate clusters. Pyroxene in these clusters consist of intergrown grains that individually have limited core-to-rim zoning, but which can differ significantly in composition between grains. Some pyroxene is possibly relict, but most crystallized from the same melt system. Compositional differences in pyroxene can be modeled as the result of a large amount (65 ± 5%) of pyroxene fractional crystallization. Clinobronzite, inclusion-rich (type 1) pyroxene, and other incompatible-element–poor (depleted type 2) pyroxene crystallized at an early stage of melt evolution, whereas incompatible-element–rich (enriched type 2) pyroxene crystallized at a later stage. Disequilibrium effects are mainly restricted to the first-formed pyroxene, which probably crystallized initially as protopyroxene, whereas later-formed pyroxene probably crystallized initially as orthopyroxene. Some Ca diffused out of the later-formed pyroxenes, and some elements (e.g., Fe, Mg) in pyroxene could have been partly homogenized as a result of a subsequent metamorphic or slow-cooling effect. Steinbach parental melts probably formed as batch melts that separated from an olivine-rich residue after ≥30–50% and probably ≥50% partial melting of an ordinary-chondrite–like protolith at ~1450–1490 °C, with silicate liquids experiencing substantial (~30–56%) FeO loss when they were hottest. We suggest that the data for IVA meteorites are best explained by a model of simultaneous endogenic heating and catastrophic collisional disruption, with disruption occurring while the parent body was substantially molten. Disruption led to a molten and outgassed IVA source body that contained metallic and silicate liquids stripped of an olivine-rich mantle.

Acknowledgments–We thank John Wasson, Nancy Chabot, Henning Haack, and Christine Floss for constructive comments that helped improve the quality of this manuscript, and Christine Floss for editorial handling. This work was supported by NASA grant NAG5-12856 (A. R.).

Editorial Handling—Dr. Christine Floss

REFERENCES

Anders E. and Grevesse N. 1989. Abundances of the elements: Meteoritic and solar. *Geochimica et Cosmochimica Acta* 53:197–214.

Andersen O. 1915. The system anorthite-forsterite-silica. *American Journal of Science* 39:407–454.

Asphaug E., Agnor C. B., and Williams Q. 2006. Hit-and-run planetary collisions. *Nature* 439:155–160.

Baker J., Bizzarro M., Eittig N., Connelly J., and Haack H. 2005. Early planetesimal melting from an age of 4.5662 Gyr for differentiated meteorites. *Nature* 436:1127–1131.

Barnes S. J. 1986. The distribution of chromium among orthopyroxene, spinel and silicate liquid at atmospheric pressure. *Geochimica et Cosmochimica Acta* 50:1889–1909.

Beattie P. 1993. The effect of partial melting of spinel peridotite on uranium series disequilibria: Constraints from partitioning studies. *Earth and Planetary Science Letters* 177:379–391.

Beattie P. 1994. Systematics and energetics of trace element partitioning between olivine and silicate melts: Implications for the natural of mineral/melt partitioning. *Chemical Geology* 117: 57–71.

Biggar G. M. 1985. Calcium-poor pyroxenes: Phase relations in the system CaO-MgO-Al_2O_3-SiO_2. *Mineralogical Magazine* 49:49–58.

Bizzarro M., Baker J. A., Haack H., and Lundagaard K. L. 2005. Rapid time scales for accretion and melting of differentiated planetesimals inferred from ^{26}Al-^{26}Mg chronometry. *The Astrophysical Journal* 632:L41–L44.

Bougalt H. and Hekinian R. 1974. Rift valley in the Atlantic ocean near 36°50′ N: Petrology and geochemistry of basaltic rocks. *Earth and Planetary Science Letters* 24:249–261.

Brearley A. J. and Jones R. H. 1998. Chondritic meteorites. In *Planetary materials,* edited by J. J. Papike. Washington, D.C.: Mineralogical Society of America. pp. 3-1–3-398.

Chen G. Q. and Ahrens T. J. 2004. High pressure and high temperature equation-of-state of gamma and liquid iron. *High-Pressure Materials Research* 499:41–61.

Chen G. Q., Ahrens T. J., and Stolper E. M. 2003. Shock wave equation of state of molten and solid fayalite. *Physics of the Earth and Planetary Interiors* 134:35–52.

Clayton R. N., Mayeda T. K., Olsen E. J., and Prinz M. 1983. Oxygen isotope relationships in iron meteorites. *Earth and Planetary Science Letters* 65:229–232.

Colson R. O., McKay G. A., and Taylor L. A. 1988. Temperature and

composition dependencies of trace element partitioning: Olivine/melt and low-Ca pyroxene/melt. *Geochimica et Cosmochimica Acta* 52:539–553.

Dick R. D., Weaver T. A., and Olinger B. 1973. Shock compression of the Webster dunite. *Eos* 54:475–476.

Dostal J., Dupuy C., Carron J. P., Le Guen de Kerneizan M., and Maury R. C. 1983. Partition coefficients of trace elements: Application to volcanic rocks of St. Vincent, West Indies. *Geochimica et Cosmochimica Acta* 37:525–533.

Duke J. M. 1976. The distribution of the period four transition elements among olivine, calcic clinopyroxene, and mafic silicate liquid. *Journal of Petrology* 17:499–521.

Dunn T. 1987. Partitioning of Hf, Lu, Ti, and Mn between olivine, clinopyroxene, and basaltic liquid. *Contributions to Mineralogy and Petrology* 96:476–484.

Dunn T. and Sen C. 1994. Mineral/matrix partition coefficients for orthopyroxene, plagioclase, and olivine in basaltic to andesitic systems: A combined analytical and experimental study. *Geochimica et Cosmochimica Acta* 58:717–733.

Ewart A. and Griffen W. L. 1994. Applications of proton-microprobe data: Trace element partitioning in volcanic rocks. *Chemical Geology* 117:251–284.

Ewart A., Bryan W. B., and Gill J. 1973. Mineralogy and geochemistry of the younger volcanic islands of Tonga, S.W. Pacific. *Journal of Petrology* 14:429–465.

Feldstein S. N., Jones R. N., and Papike J. J. 2001. Disequilibrium partial melting experiments on the Leedey L6 chondrite: Textural controls on melting processes. *Meteoritics & Planetary Science* 36:1421–1441.

Gaetani G. A. and Grove T. L. 1997. Partitioning of rare earth elements between clinopyroxene and silicate melt: Crystal-chemical controls. *Geochimica et Cosmochimica Acta* 59:1951–1962.

Gaines R. V., Skinner H. C. W., Foord E. E., Mason B., and Rosenzweig A. 1997. *Dana's new mineralogy: The system of mineralogy of James Dwight Dana and Edward Salisbury Dana,* 8th ed. New York: John Wiley & Sons. 1819 p.

Ganguly J. and Stimpfl M. 2000. Cation ordering in orthopyroxenes from two stony-iron meteorites: Implications for cooling rates and metal-silicate mixing. *Geochimica et Cosmochimica Acta* 64:1291–1297.

Ghosh A., Weidenschilling S. J., McSween H. Y., Jr., and Rubin A. 2006. Asteroidal heating and thermal stratification of the asteroid belt. In *Meteorites and the early solar system II,* edited by Lauretta D. S. and McSween H. Y., Jr. Tucson, Arizona: The University of Arizona Press. pp. 555–566.

Goldstein J. I. and Short J. M. 1967. Cooling rates of 27 iron and stony-iron meteorites. *Geochimica et Cosmochimica Acta* 31: 1001–1023.

Green T. H. 1994. Experimental studies of trace element partitioning applicable to igneous petrogenesis—Sedona 16 years later. *Chemical Geology* 117:1–36.

Haack H. and Scott E. R. D. 1992. Asteroid core crystallization by inward dendritic growth. *Journal of Geophysical Research* 97: 14,727–14,734.

Haack H., Scott E. R. D., Love S. G., Brearley A. J., and McCoy T. J. 1996. Thermal histories of IVA stony iron and iron meteorites: Evidence for asteroid fragmentation and reaccretion. *Geochimica et Cosmochimica Acta* 60:3103–3133.

Hart S. R. and Davis K. L. 1978. Nickel partitioning between olivine and silicate melt. *Earth and Planetary Science Letters* 40:203–219.

Heyse J. V. 1979. The metamorphic history of the LL group ordinary chondrites. Ph.D. thesis, State University of New York at Stony Brook, Stony Brook, New York, United States of America.

Hsieh K.-C., Vlach K. C., and Chang Y. A. 1987. The Fe-Ni-S system, I. A thermodynamic analysis of the phase equilibria and calculation of the phase diagram from 1173 to 1623 K. *High Temperature Science* 23:17–38.

Huebner J. S. 1980. Pyroxene phase equilibria at low pressure. In *Pyroxenes,* edited by Prewitt C. T. Washington, D.C.: Mineralogical Society of America. pp. 213–288.

Irving A. J. and Frey F. A. 1984. Trace element abundances in megacrysts and their host basalts: Constraints on partition coefficients and meagcryst genesis. *Geochimica et Cosmochimica Acta* 48:1201–1221.

Jarosewich E. 1990. Chemical analyses of meteorites: A compilation of stony and iron meteorite analyses. *Meteoritics* 25:323–337.

Jones R. H. and Layne G. D. 1997. Minor and trace element partitioning between pyroxene and melt in rapidly cooled chondrules. *American Mineralogist* 82:534–545.

Jurewicz A. J. G., Mittlefehldt D. W., and Jones J. H. 1993. Experimental partial melting of the Allende (CV) and Murchison (CM) chondrites and the origin of asteroidal basalts. *Geochimica et Cosmochimica Acta* 57:2123–2139.

Jurewicz A. J. G., Mittlefehldt D. W., and Jones J. H. 1995. Experimental partial melting of the St. Severin (LL) and Lost City (H) chondrites. *Geochimica et Cosmochimica Acta* 59:391–408.

Keleman P. B. and Dunn J. T. 1992. Depletion of Nb relative to other highly incompatible elements by melt/rock reaction in the upper mantle. *Eos* 73:656–657.

Keil K. and Wilson L. 1993. Explosive volcanism and the compositions of cores of differentiated asteroids. *Earth and Planetary Science Letters* 117:111–124.

Kennedy A. K., Lofgren G. E., and Wasserburg G. J. 1993. An experimental study of trace element partitioning between olivine, orthopyroxene and melt in chondrules: Equilibrium values and kinetic effects. *Earth and Planetary Science Letters* 115:177–195.

Kent A. J. R., Jacobsen B., Peate D. W., Waight T. E. and Baker J. A. 2004. Isotope dilution MC-ICP-MS rare earth element analysis of geochemical reference materials NIST SRM 610, NIST SRM 612, NIST SRM 614, BHVO-2G, BHVO-2, BCR-2G, JB-2, WS-E, W-2, AGV-1 and AGV-2. *Geostandards and Geoanalytical Research* 28:417–429.

Klock W. and Palme H. 1988. Partitioning of siderophile and chalcophile elements between sulfide, olivine, and glass in a naturally reduced basalt from Disko Island, Greenland. Proceedings, 18th Lunar and Planetary Science Conference. pp. 471–483.

Kubaschewski O. 1982. *Iron-binary phase diagrams.* Berlin: Springer-Verlag. 185 p.

Larsen L. M. 1979. Distribution of REE and other trace elements between phenocrysts and peralkaline undersaturated magmas, exemplified by rocks from the Gardar igneous province, south Greenland. *Lithos* 12:303–315.

Leeman W. P. and Scheidegger K. F. 1976. Olivine/liquid distribution coefficients and a test for crystal-liquid equilibrium. *Earth and Planetary Science Letters* 35:247–257.

Lide D. R., editor. 1990. *CRC handbook of chemistry and physics,* 71st ed. Baton Rouge, Louisiana: CRC Press. 2233 p.

Lodders K. and Fegley B., Jr. 1998. *The planetary scientist's companion.* New York: Oxford University Press. 371 p.

Longhi J. 1991. Comparative liquidus equilibria of hypersthene-normative basalts at low pressure. *American Mineralogist* 76: 785–800.

Marvin U. B., Petaev M. I., Croft W. J., and Killgore M. 1997. Silica minerals in the Gibeon IVA iron meteorite (abstract #1374). 28th Lunar and Planetary Science Conference. CD-ROM.

McCoy T. J., Mittlefehldt D. W., and Wilson L. 2006. Asteroid differentiation. In *Meteorites and the early solar system II,* edited by Lauretta D. S. and McSween H. Y., Jr. Tucson, Arizona: The University of Arizona Press. pp. 733–745.

McKay G. A. and Weill D. F. 1976. Petrogenesis of KREEP. Proceedings, 7th Lunar Science Conference. pp. 2427–2447.

McKay G. A. and Weill D. F. 1977. KREEP petrogenesis revisited. Proceedings, 8th Lunar Science Conference. pp. 2339–2355.

McKay G., Wagstaff J., and Yang S.-R. 1986. Zirconium, hafnium, and rare earth element partition coefficients for ilmenite and other minerals in high-Ti lunar mare basalts: An experimental study. Proceedings, 16th Lunar and Planetary Science Conference. pp. D229–D237.

Miller G. H., Stolper E. M., and Ahrens T. J. 1991. The equation of state of a molten komatiite. 1. Shock wave compression to 36 GPa. *Journal of Geophysical Research* 96:11,831–11,848.

Moren A. E. and Goldstein J. I. 1978. Cooling rate variations of group IVA iron meteorites. *Earth and Planetary Science Letters* 40: 151–161.

Moren A. E. and Goldstein J. I. 1979. Cooling rates of group IVA iron meteorites determined from a ternary Fe-Ni-P model. *Earth and Planetary Science Letters* 43:182–196.

Morse S. A. 1980. *Basalts and phase diagrams—An introduction to the quantitative use of phase diagrams in igneous petrology.* New York: Springer-Verlag. 493 p.

Mysen B. 1976. Experimental determination of nickel partition coefficients between liquid, pargasite and garnet peridotite minerals and concentration limits of behavior according to Henry's Law at high pressure and temperature. *American Journal of Science* 278:217–243.

Nielsen R. L., Gallahan W. E., and Newberger F. 1992. Experimentally determined mineral-melt partition coefficients for Sc, Y, and REE for olivine, orthopyroxene, pigeonite, magnetite, and ilmenite. *Contributions to Mineralogy and Petrology* 110:488–499.

Paster T. P., Schauwecher D. S., and Haskin L. A. 1974. The behavior of some trace elements during solidification of the Skaergaard layered series. *Geochimica et Cosmochimica Acta* 38:1549–1577.

Pearce J. G., Perkins W. T., Westgate J. A., Gorton M. P., Jackson S. E., Neal C. R., and Chenery S. P. 1997. A compilation of new and published major and trace element data for NIST SRM 610 and NIST SRM 612 glass reference materials. *Geostandards and Geoanalytical Research* 21:15–144.

Rasmussen K. L. 1982. Determination of the cooling rates and nucleation histories of eight group IVA iron meteorites using local bulk Ni and P variation. *Icarus* 52:444–453.

Rasmussen K. L., Ulff-Møller R. F., and Haack H. 1995. The thermal evolution of IVA iron meteorites: Evidence from metallographic cooling rates. *Geochimica et Cosmochimica Acta* 59:3049–3059.

Reid A. M., Williams R. J., and Takeda H. 1974. Coexisting bronzite and clinobronzite and the thermal evolution of the Steinbach meteorite. *Earth and Planetary Science Letters* 22:67–74.

Rigdin S. M., Ahrens T. J., and Stolper E. M. 1989. High-pressure equation of state of molten anorthite and diopside. *Journal of Geophysical Research* 94:9508–9522.

Rollinson H. 1993. *Using geochemical data: Evaluation, presentation, interpretation.* Harlow, United Kingdom: Longman. 352 p.

Rowan L. R. and Ahrens T. J. 1994. Observations of impact-induced molten metal-silicate partitioning. *Earth and Planetary Science Letters* 122:71–88.

Ruzicka A., Fowler G. W., Snyder G. A., Prinz M., Papike J. J., and Taylor L. A. 1999. Petrogenesis of silicate inclusions in the Weekeroo Station IIE iron meteorite: Differentiation, remelting, and dynamic mixing. *Geochimica et Cosmochimica Acta* 63: 2123–2143.

Ruzicka A., Hutson M., and Floss C. 2006. Petrology of silicate inclusions in the Sombrerete ungrouped iron meteorite: Implications for the origins of IIE-type silicate-bearing irons. *Meteoritics & Planetary Science* 41:1797–1931.

Scott E. R. D., Haack H., and McCoy T. J. 1996. Core crystallization and silicate-metal mixing in the parent body of the IVA iron and stony-iron meteorites. *Geochimica et Cosmochimica Acta* 60: 1615–1631.

Schaudy R., Wasson J. T., and Buchwald V. F. 1972. The chemical classification of iron meteorites—VI. A reinvestigation of irons with Ge concentrations lower than 1 ppm. *Icarus* 17: 174–192.

Schwandt C. and McKay G. 1998. Rare earth element partition coefficients from enstatite/melt synthesis experiments. *Geochimica et Cosmochimica Acta* 62:2845–2848.

Solomon M. 1963. Counting and sampling errors in modal analysis by point counter. *Journal of Petrology* 4:367–382.

Takahashi E. 1978. Partitioning of Ni^{2+}, Co^{2+}, Fe^{2+}, Mn^{2+}, and Mg^{2+} between olivine and silicate melts: Compositional dependence of partition coefficient. *Geochimica et Cosmochimica Acta* 42: 1829–1844.

Turcotte D. L. and Schubert G. 1982. *Geodynamics: Applications of continuum physics to geological problems.* New York: John Wiley & Sons. 450 p.

Ulff-Møller F., Rasmussen K. L., Kallemeyn G. W., Prinz M., Palme E. H., and Spettel B. 1995. Differentiation of the IVA parent body: Evidence from silicate-bearing iron meteorites. *Geochimica et Cosmochimica Acta* 59:4713–4728.

Ulmer P. 1989. Partitioning of high field strength elements among olivine, pyroxenes, garnet and calc alkaline picrobasalt: Experimental results and an application. *International Journal of Mass Spectrometry and Ion Physics* 42–47.

Villemant B., Jaffrezic H., Joran J.-L., and Treuil M. 1981. Distribution coefficients of major and trace elements: Fractional crystallization in the alkali basalt series of Chaine des Puys (Massif Central, France). *Geochimica et Cosmochimica Acta* 45: 1997–2016.

Voshage H. and Feldmann H. 1979. Investigations on cosmic-ray–produced nuclides in iron meteorites, 3. Exposure ages, meteoroid sizes and sample depths determined by mass spectrometric analysis of potassium and rare gases. *Earth and Planetary Science Letters* 45:293–308.

Wadwha M., Srinivasan G., and Carlson R. W. 2006. Time scales of planetesimal differentiation in the early solar system. In *Meteorites and the early solar system II,* edited by Lauretta D. S. and McSween H. Y., Jr. Tucson, Arizona: The University of Arizona Press. pp. 715–731.

Wang P.-I., Rumble D. III, McCoy T. J. 2004. Oxygen isotopic compositions of IVA iron meteorites: Implications for the thermal evolution derived from in situ ultraviolet laser microprobe analyses. *Geochimica et Cosmochimica Acta* 68: 1159–1171.

Wasson J. T. and Richardson J. W. 2001. Fractionation trends among IVA iron meteorites: Contrasts with IIIAB trends. *Geochimica et Cosmochimica Acta* 65:951–970.

Wasson J. T., Matsunami Y., and Rubin A. E. 2006. Silica and pyroxene in IVA irons: Possible formation of the IVA magma by impact melting and reduction of L-LL chondrite materials followed by crystallization and cooling. *Geochimica et Cosmochimica Acta* 70:3149–3172.

Watson E. B. 1977. Partitioning of Mn between forsterite and silicate liquid. *Geochimica et Cosmochimica Acta* 41:1363–1374.

Weill D. F. and McKay G. A. 1975. The partitioning of Mg, Fe, Sr,

Ce, Sm, Eu, and Yb in lunar igneous systems and a possible origin of KREEP by equilibrium partial melting. Proceedings, 6th Lunar Science Conference. pp. 1143–1158.

Yang J., Goldstein J. I., and Scott E. R. D. 2006. Evolution of differentiated asteroids as inferred from cooling rates of magmatic iron meteorites. *Meteoritics & Planetary Science* 41: A193.

Yang J., Goldstein J. I., and Scott E. R. D. Forthcoming. Metallographic cooling rates and origin of IVA iron meteorites. *Geochimica et Cosmochimica Acta.*

APPENDIX

Table A1. Data for glass standards NIST 612, BCR-2G, and BHVO-2G, and for low-Ca pyroxene in Steinbach, relevant for evaluating LA-ICP-MS analysis quality. See text.

	3σ detection limit (ng/g)[a]	Precision BCR-2G (%)[b]	Precision BHVO-2G (%)[b]	Accuracy BCR-2G (%)[c]	Accuracy HVO-2G (%)[c]	Pyroxene counting error (ng/g)[d]
Al	3350	6.5	2.7	8.5	21.5	2690
Si	18,800	–	–	–	–	167,000
Ca	12,400	1.2	0.8	12.1	3.5	36,600
Sc	52.3	1.9	2.4	10.5	10.7	74.1
Ti	219	1.0	0.7	7.2	20.0	1130
V	7.75	4.5	1.0	9.4	9.5	219
Cr	267	10.3	1.0	5.3	4.1	4690
Mn	26.3	0.5	1.7	40[e]	34[e]	1160
Co	33.4	2.5	5.6	16.0	8.6	146
Ni	502	215	15.2	–	14.0	4120
Zn	27.5	4.2	1.9	2.5	0.4	33.1
Ga	18.3	2.0	1.4	135	31.1	9.9
Rb	16.1	2.3	1.3	10.5	12.3	16.3
Sr	7.23	3.8	2.2	18.4	4.9	6.5
Y	4.56	7.4	3.6	28.8	2.2	13.0
Zr	11.6	7.2	3.0	27.0	3.2	19.1
Nb	2.28	3.8	3.1	–	11.1	5.1
Cs	9.88	7.0	22.4	3.3	–	7.3
Ba	37.8	1.8	3.8	13.1	1.9	49.5
La	4.22	3.3	3.0	12.6	7.4	7.2
Ce	1.60	1.1	3.0	14.3	5.2	4.0
Pr	1.47	3.5	5.6	14.9	0.0	2.9
Nd	4.43	3.1	3.3	13.9	5.2	14.8
Sm	5.67	8.0	3.0	15.1	4.5	22.2
Eu	2.18	5.0	3.4	11.1	5.8	6.4
Gd	15.4	7.5	3.8	9.3	3.7	31.1
Tb	1.08	5.9	5.1	22.2	5.3	3.3
Dy	3.33	5.4	5.5	16.2	2.0	11.4
Ho	1.07	6.7	3.4	17.2	7.5	3.5
Er	2.45	5.6	6.9	17.3	5.8	8.1
Tm	1.14	7.0	5.5	18.2	–	2.8
Yb	3.26	5.4	10.8	10.1	5.7	13.0
Lu	1.16	8.6	5.3	12.0	1.4	3.0
Hf	2.41	5.6	7.0	19.2	2.8	9.2
Th	0.798	4.8	3.4	7.3	4.0	5.8
U	0.411	3.7	12.0	3.9	–	2.0

[a]Detection limit (*DL*) related to 3 × standard deviation of pre-shot background count fluctuation on NIST 612 standard, the principal standard used in this study (average of 17 analyses).

[b]Precision equated to coefficient of variation in measured concentrations of BCR-2G analyzed as unknown (6 analyses) and of BHVO-2G analyzed as unknown (3 analyses), using NIST 612 as the standard.

[c]Difference between measured and reported concentrations for BCR-2G and BHVO-2G: accuracy = 100 × | measured - reported|/[reported].

[d]Average 1σ error for low-Ca pyroxene in Steinbach based on counting statistics.

[e]Unrealistically high values reflect data dropouts caused by saturation of the detector.

Table A2. Low-Ca pyroxene (px) and olivine (ol) crystal/liquid partition coefficients (*D* values) assumed in models. Values after "±" represent standard deviations of averaged values.

	$D^{px/liq}$	References[a]	$D^{ol/liq}$	References[a]
Al	0.043 ± 0.014	1, 2	0.0082 ± 0.0036	1, 2, 12
Ca	0.066 ± 0.018	1, 2, 3	0.028 ± 0.004	1, 2, 12, 13, 14
Sc	0.57	1	0.22 ± 0.05	1, 4, 12, 13, 15, 16
Ti	0.082 ± 0.017	2, 3, 4	0.021 ± 0.009	2, 4, 14, 15, 18
V	0.89 ± 0.29	2, 4, 5	0.12 ± 0.09	2, 4, 18, 19, 20, 21
Cr	0.51	6	0.96 ± 0.30	2, 12, 15, 16, 18, 19, 21
Mn	0.85 ± 0.39	1, 2, 3	1.0 ± 0.3	1, 2, 12, 13, 14, 18, 20, 21, 22, 23
Co	1.03	2	3.6 ± 1.4	2, 12, 13, 15, 18, 19, 20, 22, 24, 25
Ni	1.1 ± 0.1	2, 7	11.9 ± 5.7	2, 13, 15, 17, 18, 19, 20, 21, 22, 26
Sr	0.0062 ± 0.0049	2, 3, 8, 9	0.0014 ± 0.0013	2, 12, 16, 27
Y	0.017 ± 0.008	2, 3, 4	0.0071 ± 0.0026	2, 12, 28
Zr	0.017 ± 0.010	2, 3, 4, 8	9.5 E-4 ± 4.5 E-5	2, 29
Nb	0.0080 ± 0.0036	2, 4, 8	0.0041 ± 0.0037	2, 29, 30
Ce	0.0028 ± 0.0020	2, 3, 10, 11	5.30 E-5 ± 1.60 E-5	2, 12
Nd	0.0056 ± 0.0027	2, 3, 10, 11	2.70 E-4 ± 4.50 E-5	2, 12
Dy	0.033 ± 0.016	2, 3, 10, 11	0.0029 ± 0.0002	2, 12
Ho	0.043	Interpolated Dy-Er	0.0079 ± 0.0010	2, 12
Er	0.052 ± 0.026	2, 3, 10, 11	0.012 ± 0.001	2, 12
Yb	0.083 ± 0.054	2, 3, 10, 11	0.028 ± 0.004	2, 12
Lu	0.099	Extrapolated Er-Yb	0.036 ± 0.006	2, 12

[a]References: (1) Colson et al. (1988); (2) Kennedy et al. (1993); (3) Jones and Layne (1997); (4) Ulmer (1989); (5) Ewart et al. (1973); (6) This study, inferred from Cr-Al co-variation and assuming D_{Al} = 0.043; (7) Mysen (1976); (8) Keleman and Dunn (1992); (9) Weill and McKay (1975); (10) Irving and Frey (1984); (11) Schwandt and McKay (1998); (12) Beattie (1994); (13) Leeman and Scheidegger (1976); (14) Dunn (1987); (15) Klock and Palme (1998); (16) McKay and Weill (1976, 1977); (17) Ewart and Griffin (1994); (18) Bougalt and Hekinian (1974); (19) Dostal et al. (1983); (20) Duke (1976); (21) Gaetani and Grove (1997); (22) Takahashi (1978); (23) Watson (1977); (24) Paster et al. (1974); (25) Villemant et al. (1981); (26) Hart and Davis (1978); (27) Beattie (1993); (28) Nielsen et al. (1992); (29) Larsen (1979); (30) Dunn and Sen (1994).